New constraints on the chronology, magnitude, and distribution of deformation within the central Andean orocline

Nathan Eichelberger,[1] Nadine McQuarrie,[2] Todd A. Ehlers,[3] Eva Enkelmann,[4] Jason B. Barnes,[5] and Richard O. Lease[3,6]

Received 1 November 2012; revised 5 April 2013; accepted 1 August 2013.

[1] Constructing an accurate kinematic model for crustal thickening in the central Andes is hampered by the inability of 2-D balanced cross sections to resolve the 3-D displacement field within the poorly studied orocline core. This study presents new structural and thermochronometer data from the orocline axis in the central Andes that constrains the magnitude and timing of deformation through (1) a balanced cross section quantifying shortening perpendicular to strike, (2) field observations that constrain translational displacements parallel to strike, and (3) thermochronology that brackets the age of exhumation and deformation. Mapping results show that north directed, right-lateral motion has been accommodated on at least one major strike-slip fault in the Eastern Cordillera (EC). Shortening perpendicular to fault strike is ~179 km (41%) for the EC and inter-Andean zone (IA) and ~86 km (39%) for the sub-Andes (SA). Apatite fission track cooling ages indicate rapid EC/IA exhumation from 46 to 18 Ma and 15 to 0 Ma in the SA. Zircon and apatite (U-Th)/He ages show that rapid exhumation began 10–5 Ma in the SA. These results are integrated with existing paleomagnetic and GPS rotation data in map view reconstructions to quantify the magnitude of translational faulting related to oroclinal bending. The reconstructions suggest that at least 85 km of north directed translational displacement has been accommodated within the orocline core. Orogen-parallel displacement and vertical axis rotations have focused crustal thickening at the orocline core and facilitated development of a high-elevation plateau, suggesting a genetic link between large-scale oroclines and plateaus.

Citation: Eichelberger, N., N. McQuarrie, T. A. Ehlers, E. Enkelmann, J. B. Barnes, and R. O. Lease (2013), New constraints on the chronology, magnitude, and distribution of deformation within the central Andean orocline, *Tectonics*, *32*, doi:10.1002/tect.20073.

1. Introduction

[2] Arcuate fold-thrust belts are common components of high plateau margins, and the most common modern examples include the Himalayas and the central Andes. Curved orogens have occurred throughout Earth history (e.g., the Appalachians, Sevier, Variscan) [*Rogers*, 1975; *Marshak*, 2004; *Weil and Sussman*, 2004; *Gutièrrez-Alonso et al*., 2012], and orocline formation has been linked with lithospheric delamination [*Gutiérrez-Alonso et al*., 2004] which has been proposed to be a key process in high plateau formation [*England and Houseman*, 1989]. Considerable effort has been directed at understanding the evolution of modern orogenic plateaus due to their proposed impacts on a diverse range of Earth systems, ranging from mantle dynamics [*Houseman et al*., 1981; *Garzione et al*., 2008] to climate [*Prell and Kutzbach*, 1992; *Poulsen et al*., 2010; *Barnes et al*., 2012] and biodiversity [*Hoorn et al*., 2010]. In the Andes, the high, internally drained Altiplano Plateau is kinematically linked to the deformation history of the adjacent Bolivian orocline [*McQuarrie and DeCelles*, 2001]. However, the kinematics of the orocline complicates applying 2-D kinematic histories [e.g., *Isacks*, 1988; *Allmendinger et al*., 1997; *Barnes et al*., 2008; *McQuarrie et al*., 2008] to constrain the 3-D deformational system affecting crustal thickening and, ultimately, plateau evolution. Documenting all kinematic factors (such as translation, rotation, and internal strain [*Yonkee and Weil*, 2010]) that contribute to the crustal budget for the Andean Plateau requires an orocline-scale reconstruction that at a minimum considers vertical axis rotations and bulk displacements parallel and perpendicular to strike. Here we present new data from the orocline axis that allows us to integrate existing results from the orocline limbs into a more complete model of the regional kinematics. This model combines across-strike shortening estimates, existing vertical axis rotations, and newly mapped

Additional supporting information may be found in the online version of this article.

[1]Department of Geosciences, Princeton University, Princeton, New Jersey, USA.
[2]Department of Geology and Planetary Science, University of Pittsburgh, Pittsburgh, Pennsylvania, USA.
[3]Department of Geosciences, University of Tübingen, Tübingen, Germany.
[4]Department of Geology, University of Cincinnati, Cincinnati, Ohio, USA.
[5]Department of Geological Sciences, University of North Carolina at Chapel Hill, Chapel Hill, North Carolina, USA.
[6]Now at U.S. Geological Survey, Anchorage, Alaska, USA.

Corresponding author: N. Eichelberger, Department of Geosciences, Princeton University, Guyot Hall, Princeton, NJ 08544, USA. (neichelb@princeton.edu)

0278-7407/13/10.1002/tect.20073

translational displacements. The model is simplified to focus on first-order structures and determine the role of translational displacements in the 3-D deformation system at the central Andean orocline.

[3] *Carey* [1955] coined the term "Bolivian orocline" and hypothesized that the distinct change in topographic and structural trend was the result of bending an initially straight orogen. By correlating fold-thrust belt width to shortening magnitude, *Isacks* [1988] proposed that a shortening gradient characterized by maxima at the orocline axis and less shortening to the north and south gradually produced the orogenic curvature. If true, this model requires a 100–250 km shortening differential between the core and limbs to produce the orocline as it exists today (Figure 1a) [e.g., *Isacks*, 1988; *Kley and Monaldi*, 1998]. However, horizontal shortening estimates from the northern limb [*McQuarrie*, 2002; *McQuarrie et al*., 2008] and the southern limb [*Elger et al*., 2005; *Kley*, 1996; *McQuarrie*, 2002; *Mueller et al*., 2002] do not support a significant gradient within Bolivia. At a larger scale, up to 150–170 km of differential shortening is possible between the northern limit of the central Andean orocline at 12–14°S (southern Peru) to northern Bolivia (15–17°S) and the Puna region of Argentina (~30°S) to southern Bolivia (~21°S) [*Coutand et al*., 2001; *Gotberg et al*., 2010]. In addition to variable shortening at a regional level, the central Andes exhibits a pattern of counterclockwise rotations north of the orocline axis and clockwise rotations to the south (Figure 1b) [*Arriagada et al*., 2006; *Barke et al*., 2007; *Roperch et al*., 2006; *Roperch et al*., 2011; *Somoza et al*., 1996]. This central Andean rotation pattern (CARP) [*Beck*, 2004] reflects a combination of block rotations related to differential shortening, radial material displacement paths [*Barke et al*., 2007; *Arriagada et al*., 2008; *Gotberg et al*., 2010], and local strain partitioning [e.g., *Riller and Oncken*, 2003]. The GPS-derived displacement field suggests that the curvature of the orocline is still developing via material displacement paths that converge toward the orocline core [*Allmendinger et al*., 2005; *Lamb*, 2000]. CARP, GPS data, and shortening estimates all emphasize that structures within the orocline core in Bolivia are a critical component of the orocline kinematic system. Prior models [e.g., *Hindle et al*., 2005; *Kley*, 1999] have proposed kinematic scenarios of orocline formation, but the lack of structural data to support or refute the models left them largely untested.

[4] Map view kinematic models predict that distributed orogen-parallel displacements (parallel to strike) are required to reconcile the divergent displacement paths of the orocline limbs (indicated by fault orientation) in the absence of outer arc extension at the foreland [*Kley*, 1999]. While map view numerical restoration of CARP data indicates that ~400 km of strike-perpendicular shortening is required at the orocline axis to reproduce the observed rotation pattern [*Arriagada et al*., 2008], strike-parallel displacements may accommodate material transport equivalent to 40% of orogen-perpendicular shortening [*Hindle et al*., 2005].

[5] Available field studies do not always agree with the shortening magnitude and displacement predictions of the orocline models. For example, *Sempere et al*. [2002] argued for the existence of N-S oriented, right-lateral faults related to Late Permian-Jurassic rifting, but without definitive displacements. *Kley* [1999] modeled significant translation along fault zones oriented oblique to the structural fabric, but acknowledged limited observational support for the structures. Recently published tectonic histories for the central Andes [e.g., *Barnes et al*., 2008; *Ege et al*., 2007; *McQuarrie et al*., 2008] integrate estimates of shortening, deformation, and exhumation across the entire eastern fold-thrust belt where consistent structural orientation supports the assumption of 2-D plane strain deformation. These studies do not address the translational displacements predicted in *Kley*'s [1999] reconstruction or the issue of map view kinematic consistency between cross-section view restorations of the orocline limbs. Using 2-D shortening estimates in a map view reconstruction can test the regional consistency and strain compatibility between balanced cross sections [e.g., *McQuarrie and Wernicke*, 2005]. Comparing the available 2-D kinematic constraints from Bolivia in map view indicates that they are insufficient to accurately model orocline formation (Figure 1d). In Figure 1d, thrust sheets are represented by polygons whose boundaries are defined by surface fault traces (Figure 1c). Each thrust sheet is sequentially displaced to a pre-Andean deformation paleoposition based on magnitude and age of shortening from balanced cross sections in the orocline limbs [*McQuarrie*, 2002; *McQuarrie et al*., 2008; *Mueller et al*., 2002]. Displacement paths are assumed to be perpendicular to structural trend, implied by the plane strain assumption of balanced cross sections. Thus, the polygon restoration paths change from SW directed vectors in the northern limb to W directed vectors in the southern limb. Strain incompatibilities arise where thrust sheets restore to overlapping paleopositions (red regions, Figure 1d). Vertical axis rotations were not considered in this model in order to isolate locations where strain compatibility is violated as the result of the plane strain assumption. The localization of strain incompatibilities at the orocline core highlights that the kinematics of the limbs is not applicable in the core region (Figure 1d). Despite the importance of the core region to understanding orocline formation, there are little data constraining its structural evolution. Here we present new map data, shortening estimates, and cooling histories that collectively define the more unique kinematics of the orocline core. These data are incorporated into a simplified map view reconstruction that provides an estimate of the magnitude of orogen-parallel displacement accommodated at the central Andean orocline.

2. Background

2.1. Bolivian Orocline Morphology

[6] The Bolivian orocline is defined by an ~50° change in orientation of the central Andes from NW-SE in Peru and northern Bolivia (the northern limb) to N-S in southern Bolivia and northern Argentina (the southern limb) (Figure 1). The morphology of the central Andes can be divided into physiographic units that are continuous throughout the orocline. From west to east, they are the Western Cordillera (WC), Altiplano (AP) basin, Eastern Cordillera (EC), inter-Andean zone (IA), and sub-Andes (SA) (Figure 1) [*Isacks*, 1988; *Kley*, 1996]. The WC is the modern volcanic arc with peak elevations of ~6 km and the western boundary of the ~3.8 km high, internally drained AP basin [*Isacks*, 1988]. In the axial region east of the AP, the EC has peak elevations of 5–6 km that are composed of Paleozoic, Mesozoic, and limited Tertiary rock deformed by west vergent folds and faults at the AP-EC boundary. Structural vergence direction in the EC switches from west (back thrust) to east (forethrust) toward the EC-IA border. The

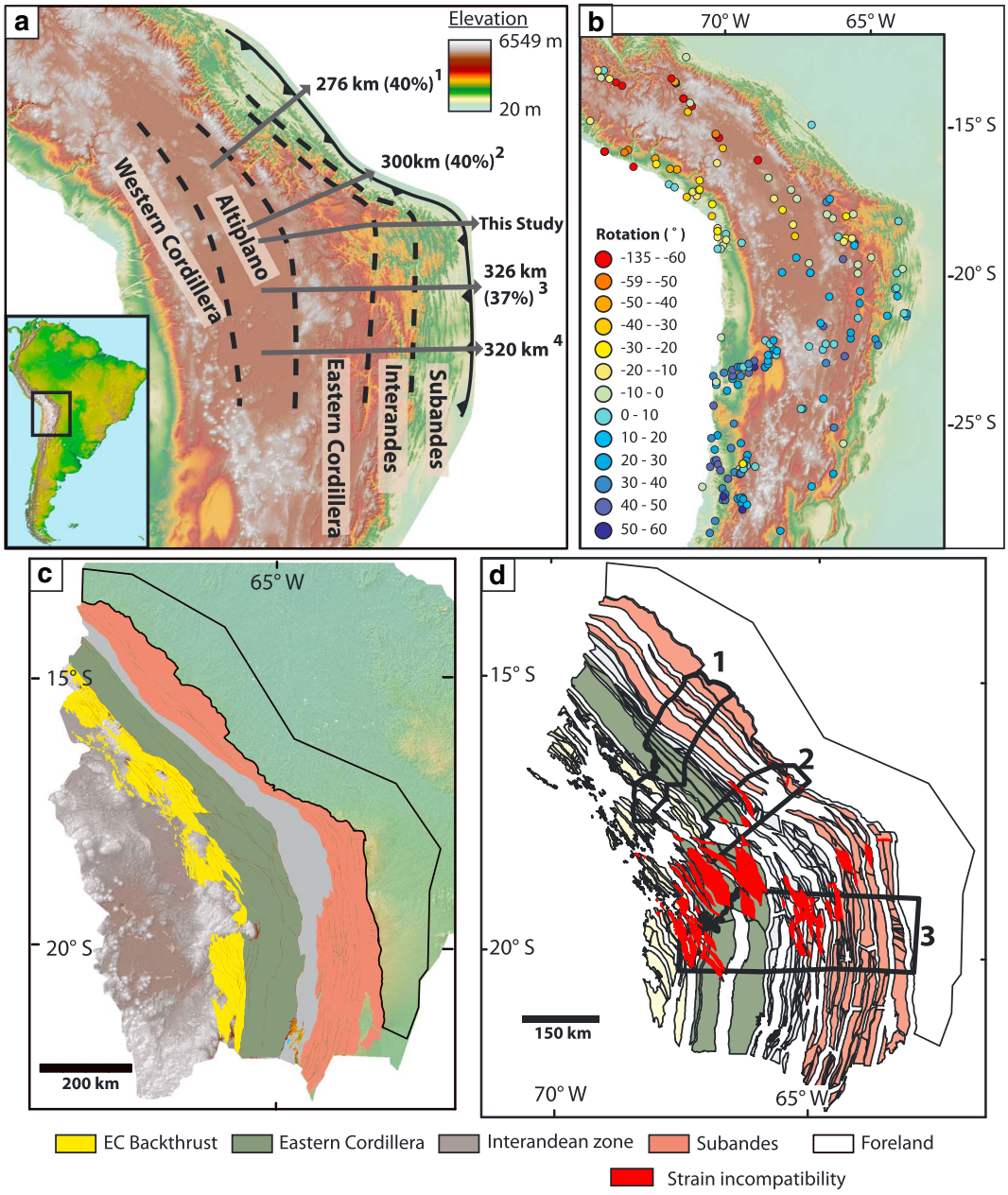

Figure 1. Topography and kinematic variation across the central Andean orocline. (a) Topography of the central Andes (GTOPO30 1 km DEM) with dashed lines separating the physiographic units at the orocline. Grey arrows represent the location and shortening direction of published shortening estimates and kinematic histories. (1) *McQuarrie et al*. [2008], (2) northern and (3) southern sections of *McQuarrie* [2002], and (4) total shortening estimate compiled from *Elger et al*. [2005], *Kley* [1996], and *Mueller et al*. [2002]. (b) Overview of central Andean rotation pattern (CARP) with the current paleomagnetic database for the central Andes. Topography is the same as Figure 1a but expanded to fit the database coverage. Sample locations for the northern orocline limb are from *Roperch et al*. [2006] and from *Arriagada et al*. [2006] for the southern limb (compiled in *Arriagada et al*.[2008]). Negative values indicate counterclockwise rotations, while positive values are clockwise. (c) Initial state of a high-resolution map view reconstruction composed of fault-bound polygons grouped by physiographic unit. (d) Restored state of the model in Figure 1b after sequentially removing shortening from cross sections outlined by bold black boxes (numbers correspond to references in Figure 1a). Red regions are overlapping fault blocks indicating locations where strain compatibility is violated in the reconstruction. The concentration of overlap between the southern limb and orocline core shows that cross sections alone do not accurately constrain orocline kinematics and the assumption of plane strain fails in a map view reconstruction.

IA is characterized by lower elevations of 2–3 km. The SA is the eastern limit of deformation with ranges under <2 km. Elevations decrease through the SA into the Chaco foreland basin where topographic relief diminishes to a low foreland slope [*Barnes and Heins*, 2009].

2.2. Stratigraphy

[7] The deformed rocks in the central Andes are a thick sequence of Ordovician through Tertiary metasedimentary and sedimentary rock. In both orocline limbs, the Paleozoic stratigraphy reaches a maximum thickness of ~15 km in the EC [*Sempere*, 1995; *Roeder and Chamberlain*, 1995; *Welsink et al.*, 1995] and tapers eastward toward the Brazilian shield [*Welsink et al.*, 1995] and westward across the Altiplano [*Sempere*, 1995]. This Paleozoic section is a continuous sequence of Ordovician through Devonian strata unconformably overlain by a discontinuous sequence of Carboniferous, Jurassic, and Cretaceous strata that is variably preserved [*González et al*., 1996; *Roeder and Chamberlain*, 1995; *Sempere*, 1994, 1995]. For both limbs, pre-Jurassic erosion generally increases across strike from the IA to the EC [*McQuarrie*, 2002] and is greatest in the southern limb [*McQuarrie and DeCelles*, 2001]. Tertiary synorogenic sediment exists in synclines across the width of the orogen in both limbs and attains thicknesses up to 12 km in the Altiplano, 2–4 km in the sub-Andes of the southern limb, and 6.5–7 km in the northern limb [*Baby et al*., 1995; *Dunn et al*., 1995; *Horton*, 2005; *Horton et al*., 2001; *Lamb and Hoke*, 1997; *Moretti et al*., 1996; *Sempere et al*., 1990].

2.3. Deformation and Shortening

[8] The EC, IA, and SA have accommodated the majority of shortening in the central Andes with minor shortening within the Altiplano (Figure 1c) [*Elger et al*., 2005; *Kley*, 1996; *McQuarrie*, 2002; *McQuarrie et al*., 2008; *Mueller et al*., 2002]. Deformation of the Paleozoic through Tertiary cover strata is thin skinned, but stacked basement thrusts are interpreted to be responsible for the major changes in structural elevation between the EC, IA, and SA throughout the orocline [*Kley*, 1996; *McQuarrie*, 2002; *McQuarrie et al*., 2008; *Mueller et al*., 2002]. Based on the mass balance model of balanced cross sections, the magnitude of shortening proposed for the basement must be equal to shortening mapped at the surface [*McQuarrie*, 2002]. The exact geometry and number of basement faults are debated, but basement deformation is a generally accepted model to explain the observed changes in detachment level, structural elevation, and topographic elevation [*Elger et al*., 2005; *McQuarrie*, 2002; *Mueller et al*., 2002]. Faulting and folding in the SA are constrained by seismic and borehole data which indicate that deformation is accommodated only within the Paleozoic and younger rocks [*Baby et al*., 1992; *Baby et al*., 1995; *Dunn et al*., 1995; *Watts et al*., 1995].

2.4. Vertical Axis Rotations

[9] Existing paleomagnetic data extend from 10°S to 30°S and define the CARP (Figure 1b) [*Arriagada et al*., 2006, 2008; *Roperch et al*., 2006, 2011; *Somoza et al*., 2012]. Rotations range from 0° to 50° with the largest magnitude rotations in the forearc [*Arriagada et al*., 2006; *Roperch et al*., 2006; *Taylor et al*., 2007]. Generally, larger rotations are from Oligocene and older rocks compared to units sampled that are <20 Ma [*Arriagada et al*., 2006; *Roperch et al*., 2006; *Somoza et al*., 1999]. These rotations have been interpreted to indicate that the majority of the rotation occurred between 40 and 25 Ma [*Roperch et al*., 2006].

2.5. Deformation Chronology

[10] Mineral cooling ages have been used as a timing proxy for central Andes deformation under the assumption that cooling is driven by erosional exhumation in response to the relief generated by faulting [e.g., *Barnes and Ehlers*, 2009]. In the northern limb within Bolivia, EC exhumation took place at 45–25 Ma with a later pulse at 15–0 Ma [*Barnes et al*., 2006; *Gillis et al*., 2006]. IA exhumation occurred between ~30 and 5 Ma, while the SA initiated at ~15 Ma and continues to present [*Benjamin et al*., 1987; *Barnes et al*., 2006; *Gillis et al*., 2006; *McQuarrie et al*., 2008; *Safran et al*., 2006]. Geologic constraints show that deformation in the EC had ceased by 25 Ma [*Gillis et al*., 2006; *Horton*, 2005], while climate models suggest that the younger (~15–0 Ma) exhumation phase in the EC is probably the result of enhanced orographic precipitation [*Barnes et al*., 2012]. In the southern limb, the EC was mostly exhumed from 40 to 20 Ma followed by the IA from 22 to 10 Ma and the SA from 15 to 0 Ma [*Ege et al*., 2007; *Barnes et al*., 2008; *Scheuber et al*., 2006].

3. Methods

[11] This study presents (1) new mapping compiled from field observations, (2) a new balanced cross section, and (3) new thermochronology samples from the orocline core. We describe our methods for map compilation, cross-section construction, and low-temperature thermochronologic analysis below.

3.1. Geologic Mapping

[12] Our new map was compiled in ArcGIS from our own 1:50,000 scale field maps, a database of published 1:100,000, 1:250,000, and 1:1,000,000 scale geologic maps [*Gobierno de Bolivia*, 1979a, 1979b, 1979c, 1979d; *Servicio Geologico de Bolivia*, 1992, 1993a, 1993b, 1994, 1995; *Sheffels*, 1988], a 30 m resolution Advanced Spaceborne Thermal Emission and Reflection Radiometer (ASTER) images, Digital Elevation Models (DEM), and 30 m visible-spectrum Landsat images. A single straight-line transect of observations was impossible because of limited access to the area and variable structural orientations. Instead, we focused on collecting observations from E-W (perpendicular to strike) and N-S (parallel to strike) roads to fill in the gap between previously mapped transects (transects 2 and 4 in Figure 1a) [*McQuarrie*, 2002]. Map patterns for areas without direct observations were interpreted from proximal observations, digital topography, and satellite images.

[13] Section lines for the balanced cross section were chosen by proximity to field observations and oriented normal to the structural trend, which resulted in several breaks in section due to regional changes in structural orientation. These breaks were positioned at physiographic boundaries and structures with extensive (>50 km) along-strike continuity [after *McQuarrie*, 2002; *McQuarrie et al*., 2008]. We developed a cross section at a scale of 1:100,000 pinned at the AP-EC boundary in the west and the undeformed Chaco foreland basin in the east. We do not consider deformation within the AP because of the proximity to prior shortening

estimates (<100 km to the north and south) [*McQuarrie*, 2002] and the along-strike continuity of structures that accommodate the shortening. To compare shortening estimates along strike, we include 47 km of AP shortening documented to the north and south [*McQuarrie*, 2002] in the total amount of shortening calculated for our axial study area.

3.2. Balanced Cross Section

[14] The balanced cross section is constrained by bedding orientation data, seismic data in the foreland and adjacent SA [*Dunn et al*., 1995; *Moretti et al*., 1996], stratigraphic thickness variations across the fold-thrust belt, and map view constraints on increases in structural elevation from the SA to the EC (described in section 4.1). The restored section was constructed simultaneously with the deformed section by individually restoring each thrust sheet using the sinuous bed method [*Dahlstrom*, 1969]. Bed lengths at the top and base of each thrust sheet were measured in the deformed section then plotted on the restored section by matching the bed length and thickness to the corresponding footwall cutoff. This assures that bed thickness is preserved, that restored strata lengths are equal across multiple detachment levels, and that each fault has a kinematically viable displacement path from the basal decollement to the surface [*Boyer and Elliott*, 1982; *McQuarrie et al*., 2008; *Robinson*, 2008; *Woodward et al*., 1989]. Eroded hanging wall cutoffs were projected to just above the erosion surface, thereby minimizing the length of the eroded thrust sheet and adhering to a minimum shortening estimate. Where the hanging wall cutoff is projected beyond the erosion surface, the additional length is required to maintain balance for the proposed structural geometry at depth. Subsurface fault geometries are predicted using fault bend fold [*Suppe*, 1983] and fault propagation fold [*Mitra*, 1990] models constrained by kink planes interpreted from surface dips [*Suppe*, 1983]. The cross section is oriented parallel to the thrust fault displacement direction as defined by features such as folds, faults, and axial planar cleavage. As a result, it does not account for translational displacements out of the cross-section plane.

[15] The greatest source of uncertainty in the balanced cross section is the subsurface thrust geometry used to fill the space between the decollement and surface structures. Surface structure geometry, known stratigraphic thicknesses, and location of detachment horizons make it possible to predict the probable dimensions of subsurface thrust sheets needed to fill the remaining space. Here, we modeled the subsurface thrusts as hinterland-dipping duplexes because (a) duplexing is the simplest mechanism to fill subsurface area and balance deformation mapped at the surface and (b) they have been observed in seismic images of the southern SA [*Dunn et al*., 1995]. The shortening magnitude uncertainties associated with eroded hanging wall cutoffs and blind duplex thicknesses are discussed in section 4.2.4. Regional changes in stratigraphic exposure define changes in structural elevation, which in turn constrain permissible basement thrust geometries [e.g., *Kley et al*., 1996; *McQuarrie*, 2002].

3.3. Thermochronology

[16] To define the study area cooling history, we collected bedrock samples from fine-to-medium grained sandstone and quartzite proximal to the base of thrust faults. We used apatite fission track (AFT), apatite (U-Th)/He (AHe), and zircon (U-Th)/He (ZHe) cooling age determinations because these systems record mineral cooling through 50°C to 200°C in the upper 10 km of the crust [e.g., *Reiners et al*., 2005]. Apatites and zircons were separated from samples by crushing, sieving, and using standard magnetic and heavy-liquid techniques [e.g., *Donelick et al*., 2005]. The fission track data were measured using the external detector method, and (U-Th)/He data were measured using laser heating and inductively coupled plasma-mass spectrometry (ICP-MS) (analytical details in Appendix A).

3.3.1. Fission Track

[17] Fission track thermochronology is based on the measurement of damage trails (tracks) in the crystal lattice produced by the spontaneous fission of ^{238}U [*Tagami and O'Sullivan*, 2005, and references therein]. These tracks are only preserved if the residence temperature of the crystal grain is lower than the grain's closure temperature (T_c), which is dependent on cooling rate and mineral type [*Dodson*, 1973]. For this study, we focused on apatite which has an effective closure temperature of 100–120°C and a temperature range of partial track annealing (partial annealing zone) between 60 and 120°C [e.g., *Green et al*., 1986; *Carlson et al*., 1999].

[18] A standard χ^2 variance test was used to determine the degree of grain age variance within a sample [*Galbraith*, 1981; *Green*, 1981]. Samples that pass the χ^2 test ($P(\chi^2) \geq 5\%$) are considered concordant [*Brandon et al*., 1998; *Galbraith*, 1981; *Green*, 1981], and the "pooled age" is used to represent the sample cooling age. If the grain age population fails the χ^2 test ($P(\chi^2) \leq 5\%$), the sample is considered discordant and the mean of the individual grain ages is reported. The variance in grain ages of discordant samples is greater than the observational uncertainty of track density alone, meaning the pooled age is not reflective of a uniquely interpretable geologic process [*Green*, 1981; *Tagami and O'Sullivan*, 2005]. Discordant ages are common in sedimentary rocks due incomplete thermal resetting after deposition or, in case of a reset sample, due to compositionally variable mineral populations within the sample [e.g., *Green et al*., 1986; *Crowley et al*., 1991; *Carlson et al*., 1999; *Barbarand et al*., 2003]. Due to the low spontaneous track densities on a per grain basis, we could not measure confined track lengths.

3.3.2. (U-Th)/He

[19] (U-Th)/He dating of minerals is based on measuring the accumulation of ^{4}He produced by α-decay of U and Th. The retention of ^{4}He in apatite and zircon is governed principally by temperature and time [*Ehlers and Farley*, 2003; *Farley*, 2002]. Closure temperature ranges from 50 to 75°C for apatite [*Ehlers and Farley*, 2003] and 160 to 200°C for zircon [*Reiners et al*., 2004]. We present apatite and zircon (U-Th)/He ages as the mean of three replicate samples, which allows for assessment of sample quality (e.g., problematic samples with inclusions or zonation). In unreset samples, replicate ages vary due to the detrital origin of zircons and apatites in metasedimentary rocks. For reset samples, the mean and variance of the replicate ages are reported as the cooling age and sample error because replicate age variance (~10%) exceeds uncertainty in the ICP-MS measurements (<~2%).

3.3.4. Component Ages and Thermal Modeling

[20] For discordant AFT grain age populations, component ages were determined using the program BinomFit to identify

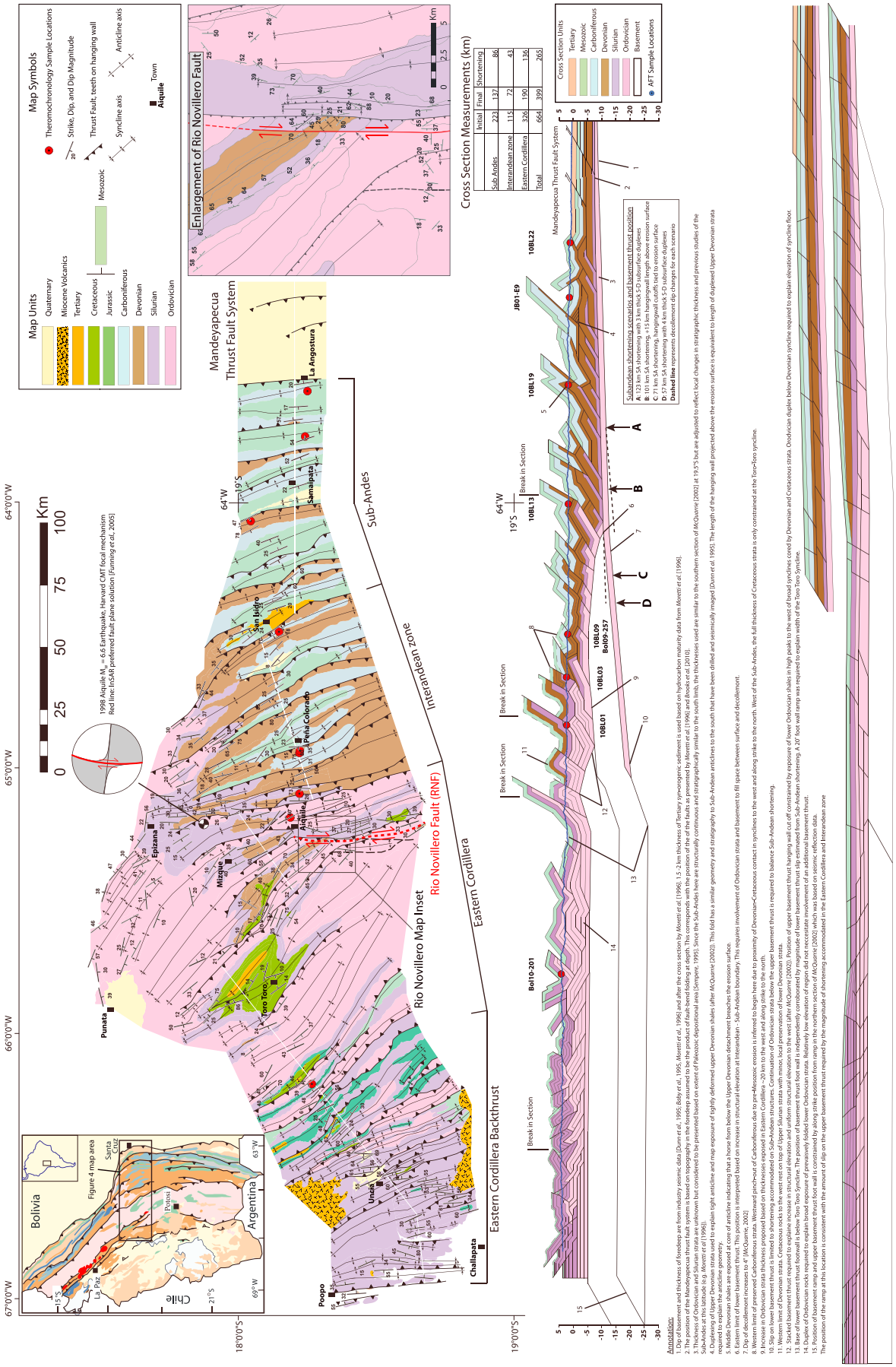

Figure 2. Geologic map and balanced cross section. A high-resolution version of this figure is available in the online PDF and as a Supporting Information file.

the significant peak ages in the sample's grain age distribution [*Brandon*, 2002]. Discordant AFT samples were classified as "mixed-reset" (MR) if all peaks were younger than deposition and "detrital" (D) if the peaks were older than deposition. "Reset" (R) samples have a single, concordant peak age younger than the depositional age [*Brandon et al*., 1998].

[21] The youngest component age for MR samples is commonly interpreted to reflect the most recent cooling event [*Brandon et al*., 1998]. For our samples, two factors argue for the use of a mean age over the young component peak age. First, all component ages are much younger than deposition and cannot be directly related to a geologic process or correlated with apatite composition. Second, the lack of track length data precluded inverse thermal modeling to determining individual AFT-based cooling histories (as in *Barnes et al*. [2006, 2008] and *McQuarrie et al*. [2008]). Instead, using a mean age and standard deviation gives a conservative estimate for the minimum onset age of rapid cooling.

[22] For a single sample (SA3), AHe, AFT, and ZHe cooling ages provided sufficient constraint to run a single thermal model using HeFTy (version 1.7.4) [*Ehlers et al*., 2005; *Ketcham*, 2005]. The mean AFT grain age and 1σ standard deviation were used in lieu of individual AFT grain ages because the sample was discordant. Track length distribution was unconstrained, and we input (U-Th)/He cooling ages with 2σ error. We imposed a starting time of 100 Ma older than the oldest, unrest cooling age for the sample, and 100°C hotter than the highest temperature thermochronometer measured [*Ketcham*, 2005]. We defined a temperature of 10–20°C at 0 Ma. Model constraints were then refined to include the depositional age (10–30°C from 420–360 Ma) and subsequent burial sufficient to reset the AHe and AFT systems, but retain a detrital ZHe age. Cooling envelope fits are classified by the common designations of good (0.5, statistical precision limit) and acceptable (0.05, passes the 95% confidence test) [*Ketcham*, 2005]. Each time-temperature path explored for the postdeposition cooling history was halved 5 times (5E) to allow for maximum flexibility [*Ketcham*, 2005]. All segments were limited to cooling rates of <40°C/Myr in episodic, monotonic t-T paths and run by Monte Carlo search with 50,000 pathways explored [after *Barnes et al*., 2008; *McQuarrie et al*., 2008].

4. Results

4.1. Geologic Map

[23] In the orocline limbs, pronounced changes in structural elevation between the physiographic zones (EC, IA, SA) and associated large-scale structural features, such as antiforms and synforms, are interpreted to be driven by basement thrusts (Figure 2) [*Kley*, 1996; *McQuarrie*, 2002; *McQuarrie et al*., 2008; *Müller et al*., 2002]. These zones continue through the orocline axial region, suggesting that the same system of basement deformation is present there. Conversely, the physiographic zones at the axis have structural orientations that vary by as much as 45° (Figure 2), indicating that the direction of displacement on thrust faults is not uniform across strike at the orocline core. This complicates quantifying shortening by planar cross sections alone and emphasizes the importance of map view reconstructions to resolve orocline kinematics. The characteristics of each zone are detailed from foreland to hinterland (east to west), in order of increasing structural complexity.

4.1.1. Chaco Foreland Basin

[24] Seismic, borehole, and hydrocarbon maturity data from the foreland basin east of the SA at 18°S show a maximum depth of 1.5–2 km with a westward 1–2° basal decollement westward toward the Andes [*Baby et al*., 1992; *Dunn et al*., 1995; *Moretti et al*., 1996]. Combined GPS and fault scarp data indicate that modern deformation is accommodated on a few N-S oriented east vergent thrust faults that extend east of the sub-Andes topographic front into the foreland but possess negligible stratigraphic offset [*Brooks et al*., 2011].

4.1.2. Sub-Andes

[25] The eastern sub-Andes (SA) adjacent to the orocline axis is characterized by N-S trending fold axes and fault traces, continuous with the structural fabric of the southern limb (Figure 2). In the western SA, structural orientation transitions to a slightly more NNW-SSE (340–350°) orientation. This small, gradual change in SA displacement direction is not accompanied by discrete structures that could accommodate translation (Figure 2) and may be a product of southern limb rotation. Immediately north of the transect, DEM and Landsat data suggest that the structural fabric gradually bends toward a NW-SE trend, implying a transition from E directed displacement at the core to the NE directed displacement of SA structures in the northern limb.

[26] The structural style of the SA is dominated by anticlines breached by east vergent thrust faults that detach in Upper Devonian stratigraphy with 1–3 km of stratigraphic separation (Figure 2). This results in footwall synclines containing Upper Cretaceous strata preserved in valleys <10 km wide. The SA here is marked by the absence of broad piggyback basins with thick Tertiary synorogenic sediment, such as the Alto Beni syncline in the north limb or numerous basins in the southern limb. Instead, the map pattern is dominated by extensive exposures of Cretaceous through Upper Devonian units and greater thicknesses of Cretaceous strata. These fault-bound synclines continue southward, increasing in width and depth [*Baby et al*., 1992; *Dunn et al*., 1995] (see also southern transect of *McQuarrie* [2002]). This shows that the SA gently plunges to the south, decreasing in structural elevation from the axial region to the southern limb. Topographic patterns suggest that the increase in exposed stratigraphic depth and structural elevation may continue around the axis of the orocline into the north limb where Cambrian, Ordovician, and Silurian rocks are involved in SA faulting [*McQuarrie*, 2002].

4.1.3. Inter-Andean Zone

[27] The IA structural fabric is oriented NNW-SSE (~340–160°), an intermediate orientation between the N-S (0–180°) structural fabric of the southern limb and the NW-SE (320–140°) orientation of the IA in the northern limb (Figure 2). The change in orientation and inferred thrust displacement direction is sufficiently gradual that no translational displacements are observed or kinematically implied.

[28] The structural elevation increase at the IA-SA boundary occurs across a thrust fault that places Middle Devonian shale over Tertiary synorogenic sediments. The boundary is expressed by a westward increase in topographic and structural elevation. Structural elevation also increases parallel to strike, progressively exposing stratigraphy as low as Middle Ordovician units, indicating a regional southward plunge

similar to the SA. The structural elevation gain (~8 km) at the SA-IA boundary is similar to the gain at the same boundary in the southern limb [*Kley*, 1996; *McQuarrie*, 2002; *Mueller et al*., 2002] but less than the elevation increase (~14 km) observed in the northern limb [*McQuarrie*, 2002; *McQuarrie et al*., 2008]. IA faults detach in Middle Devonian shale and form footwall synclines containing Carboniferous sandstone with limited Cretaceous preservation along the fold axes (Figure 2). The Carboniferous strata pinch out to the north of the map area where Cretaceous units lie in unconformable contact with Upper Devonian strata. In the field, the contact between Devonian-Cretaceous and Carboniferous-Cretaceous units is nonangular. Fault spacing ranges from 7 to 20 km with fold wavelengths of 3 to 7 km.

4.1.4. Eastern Cordillera Forethrust

[29] The structural fabric of the EC varies significantly along strike, implying large changes in the direction of shortening (assuming shortening perpendicular to strike). In the north, EC forethrust structures run parallel to those in the northern limb (between 130° and 140°, Figure 2) [*McQuarrie*, 2002]. At the southern edge of the map area, there are two structural orientation domains: (1) N-S (150–180° strike) structures extending 25–30 km west of the EC-IA border and (2) NW-SE (130–140° strike) structures that continue west of domain 1 to the Altiplano. The NW-SE oriented domain is maintained for up to ~80 km along strike based on DEM and Landsat images. This domain is defined by large-scale structures, such as the Toro Toro syncline, that parallel northern limb structures (Figure 2) [*McQuarrie*, 2002; *McQuarrie et al*., 2008]. The southeastern edge of this domain is demarcated by the oblique truncation of NW-SE trending faults and fold axes against N-S oriented, E vergent faults in the Rio Novillero Valley at ~65.25° S (Rio Novillero Fault zone, or RNF, Figure 2). This change in fault vergence suggests N-S translational displacement parallel to the RNF. Mapping of stratigraphic contacts and fold limbs show that the RNF has accommodated right-lateral motion, offsetting a syncline containing Upper Devonian strata in a 2 km wide fault sliver bound by N-S trending strands of the RNF (Figure 2, enlargement of Rio Novillero Fault). Silurian shale on the west side of the RNF shows weak top-to-the-north shear cleavage but no regional piercing points that would independently constrain the magnitude of north directed displacement. This is the only location where a discrete change in regional structural orientation occurs across a single fault that has also clearly undergone translational deformation. It argues for out-of-plane motion localized in this area.

[30] The eastern edge of the EC is defined by an increase in structural elevation of Ordovician strata over stratigraphically higher units in the IA to the east. The map pattern across the entire forethrust zone is dominated by two regional antiforms defined by continuous, high-elevation exposures of Ordovician stratigraphy separated by the ~80 km long Toro Toro syncline (Figure 2). The eastern antiform spans ~50 km and begins near the northern map limit. It then narrows southward where it is divided by several east vergent thrusts over footwall synclines containing lower Devonian quartzite. The westernmost of these three thrusts forms the eastern Toro Toro syncline limb (Figure 2). The syncline has over 1 km of topographic relief between the Ordovician strata in the eastern limb and the Tertiary beds at the valley floor, marking a significant structural elevation change. The southwestern limb of the Toro Toro syncline forms the footwall of a west vergent thrust in Upper Ordovician quartzite with ~4 km of stratigraphic offset (Figure 2). This thrust is the eastern edge of the second antiform, defined by a >20 km wide swath of tightly folded Lower Ordovician slate, shale, and siltite at ~3 km elevation.

4.1.5. Eastern Cordillera Back Thrust

[31] Structures in the EC back thrust trend ~150°, marking a transition from ~140° in the north limb back thrust [*McQuarrie*, 2002; *McQuarrie et al*., 2008] to ~160–180° in the southern limb [*McQuarrie*, 2002; *Mueller et al*., 2002]. This change in orientation is gradual compared to the N-S to NW-SE change at the RNF, and we found no evidence for translational motion.

[32] The EC back thrust is characterized by tightly folded Upper Ordovician, Silurian, and Mesozoic strata in west verging back thrusts (Figure 2). Folds range from upright to overturned with wavelengths of 2–3 km and are generally breached by steep thrust faults over footwall synclines. Tight structural spacing here indicates a relatively shallow and constant depth to the basal detachment [after *McQuarrie and DeCelles*, 2001]. Upper Ordovician quartzite is exposed along anticline axes suggesting that faults detach at the base of the Ordovician, similar to the forethrust region. Here, Mesozoic strata rest nonconformably on top of Upper Silurian quartzite and shale, consistent with a north-to-south increase in stratigraphic depth of the pre-Jurassic erosion level [*McQuarrie and DeCelles*, 2001].

4.2. Balanced Cross Section

[33] Shortening on thrust faults is the largest contributor to the displacement field in the central Andean orocline core, but translational slip on the RNF indicates that assuming only plane strain is invalid. Our map data show that the change from N-S oriented structures of the southern limb to NW-SE orientations of the northern limb occurs in the EC at the orocline core and it is accompanied by out-of-plane displacement. In light of this, we use our cross section to estimate thrust fault displacement magnitude in the SA, IA, and EC (Figure 2) for use in a map view reconstruction.

4.2.1. Sub-Andes

[34] Limited seismic, borehole, and hydrocarbon maturity data constrain the depth of the proximal foreland basin [*Moretti et al*., 1996] as well as subsurface structures such as the blind thrust faults comprising the active Mandeyapecua fault system [*Brooks et al*., 2011]. Complete seismic data for the axial SA are not available; however, mapping indicates that the structural wavelength and regional detachment horizons are similar to areas to the south where seismic data were used to construct cross sections [*Baby et al*., 1992, *Dunn et al*., 1995; *McQuarrie*, 2002]. The SA map pattern is best explained in cross section by fault propagation folds [e.g., *Mitra*, 1990] above an Upper Devonian detachment over duplexed Silurian and Lower Devonian stratigraphy at depth. The Lower Devonian and Silurian strata are not exposed at the surface, but seismic and borehole data from structures near the foreland partially constrain their thickness [*Moretti et al*., 1996]. The higher structural elevation of the Cretaceous compared to sections in the south can be explained by greater slip on subsurface faults, creating a thicker package of duplexed rocks. As a result, the axial SA has accommodated 86 km (39%) of shortening compared to estimates of 67 km (33%) [*McQuarrie*, 2002] and 60 km

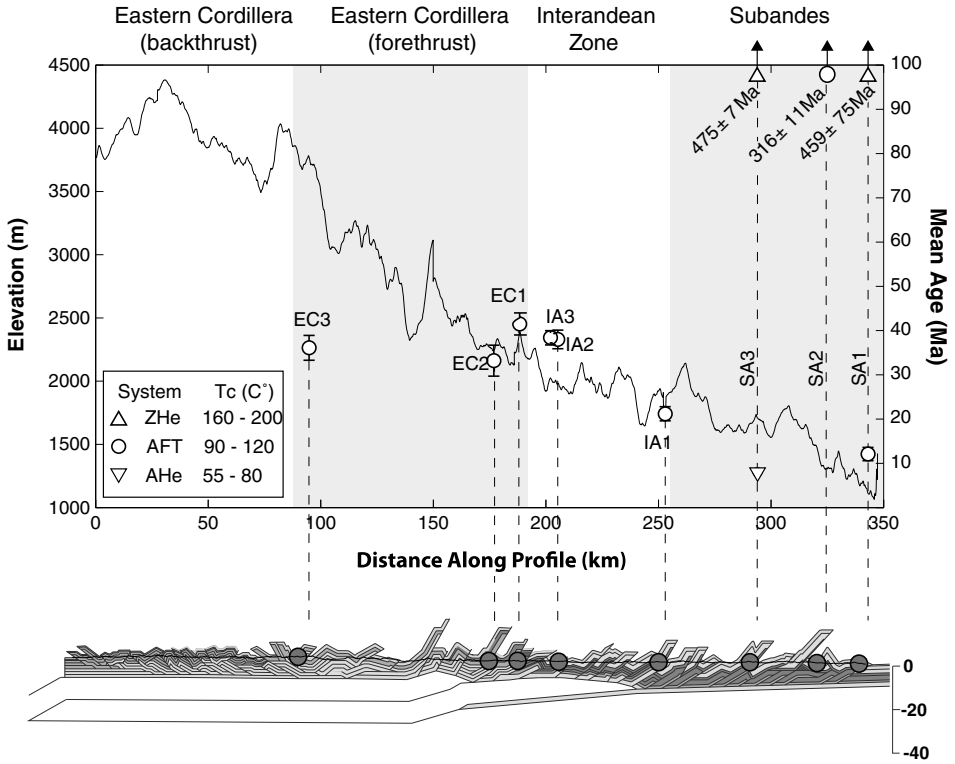

Figure 3. Topography, thermochronology data, and balanced cross section across the orocline axis (location in Figure 2). Mean elevation profile is a 50 km wide swath from ASTER 30 m DEM data. (U-Th)/He ages are the mean of three individual grain cooling ages (±2σ); AFT ages are the central age (±1σ). For sample 10BL19, the AFT and AHe ages overlap and the error bars are equivalent to symbol size for both ages. For structural reference, grey shading group samples by physiographic unit and dashed lines link position of each sample to its location on the cross section.

[*Kley*, 1996] for the SA farther south. This is equivalent to the magnitude of SA shortening reported for the orocline axis by *Barke et al*. [2007] based on joint inversion of shortening data and paleomagnetic rotations.

4.2.2. Inter-Andean Zone

[35] Deformation in the IA is similar to the SA apart from an increase in detachment elevation, inferred from the greater structural and topographic elevation of the IA [*Kley*, 1996]. The model used here follows the basement thrust solution of previous studies to explain the elevated IA detachment (Figure 2) [*Kley*, 1996; *McQuarrie*, 2002; *McQuarrie et al*., 2008]. The involvement of basement deformation in the IA is further supported by gravimetric, magnetotelluric, and seismic observations from the southern IA [*Kley et al*., 1996; *Schmitz and Kley*, 1997; *Wigger et al*., 1994]. In the cross section, the IA basement thrust thickness must accommodate the mapped increase in structural elevation while the length is limited by the magnitude of shortening accommodated in the SA (Figure 2). The basement thrust geometry we show here is a nonunique solution. An alternative geometry could involve significant basement duplexing [e.g., *Mueller et al*., 2002; *Elger et al*., 2005] to produce the same increase in structural elevation (see comparison in *McQuarrie et al*. [2008]).

4.2.3. Eastern Cordillera

[36] We explain the ~100 km wide EC structural high in the orocline axis by a second upper basement thrust [after *McQuarrie*, 2002]. We propose that the position of the Toro Toro syncline coincides with the western edge of the footwall ramp for the SA basement thrust (Figure 2). Thus, the distance between the eastern limb of the syncline and the eastern edge of the IA should equal the shortening magnitude estimated from the SA (~86 km). The structural high at the EC-IA boundary is the easternmost permissible limit for the hanging wall cutoff of the proposed upper basement thrust. Locating the upper basement thrust hanging wall cutoff here explains the structural high east of the Toro Toro syncline and the low of the syncline itself.

[37] The decrease in structural elevation at the EC-AP boundary is modeled as a basement ramp over the footwall cutoff of the upper basement thrust sheet (Figure 2) [after *McQuarrie and DeCelles*, 2001]. Since the decrease occurs immediately adjacent to the westernmost back thrust, it is treated as a regional pin line for the western edge of the thrust belt. This limits the slip on the upper basement thrust to the distance between the Altiplano pin line and the hanging wall cutoff located at the eastern EC.

4.2.4. Shortening Estimate Uncertainty

[38] *Judge and Allmendinger* [2011] have shown that stratigraphic thickness is the largest source of error in balanced cross-section shortening estimates. In the cross section presented here, stratigraphic thicknesses are best constrained in the Eastern Cordillera and Inter-Andean zone where the full range of stratigraphy is exposed and mapped. In the SA, less is known about thickness of the deformed Silurian and Devonian stratigraphy proposed to fill space between the

Table 1. Apatite Fission Track Data[a]

Sample	ID	Long	Lat	Elev. (m)	Fm. Age	n (grains)	N_s (tracks)	N_i (tracks)	ρ_s (tracks/cm^2)	ρ_i (tracks/cm^2)	ρ_d (tracks/cm^2)	χ^2 (%)	FT Age (Ma)	1σ Error	Age Range (Ma)
Sub-Andean Zone															
10BL22	SA1	−63.55	−18.18	684	Du	89	250	1987	1.74E+05	1.03E+06	6.07E+05	0	12.1	1.5	0 to 100
JB1-E9	SA2	−63.72	−18.18	1285	K	100	6048	2466	2.41E+06	9.71E+05	8.54E+05	0	316.0	11.0	129 to 715
10BL19	SA3	−64.05	−17.99	1178	Du	100	202	2361	8.42E+04	8.32E+05	6.05E+05	0	8.0	1.0	0 to 48
Inter-Andean Zone															
10BL13	IA1	−64.47	−18.10	1584	Du	100	438	1625	2.58E+05	9.40E+05	6.04E+05	0	21.2	1.6	0 to 83
10BL9	IA2	−64.92	−18.19	1859	Du	28	179	289	2.51E+05	4.84E+05	6.02E+05	0	37.7	4.6	10 to 105
Bol09-257	IA3	−64.92	−18.19	1859	Du	56	729	2343	3.96E+05	1.28E+06	8.54E+05	2	38.0	2.1	8 to 77
Eastern Cordillera															
10BL3	EC1	−65.08	−18.19	2335	S	100	1125	1913	5.70E+05	9.55E+05	6.00E+05	0	41.5	2.5	9 to 171
10BL1	EC2	−65.17	−18.16	2241	O	39	553	1313	3.09E+05	6.91E+05	5.99E+05	0	33.2	3.5	6 to 104
Bol10-201	EC3	−66.17	−18.26	4150	O	100	724	1278	5.40E+05	8.95E+05	6.08E+05	11	36.1	2.8	12 to 781

[a]Fission track ages calculated using the external detector method and zeta calibration. IRMM540 Uranium glasses are used as dosimeter for neutron irradiation. When χ^2 is >5%, then the pooled age is reported; for samples where χ^2 is <5%, the mean age is reported. N_s: number of counted spontaneous tracks, N_i: number of counted induced tracks, n: number of grains counted, ρ_s, ρ_i: spontaneous and induced track density, ρ_d: induced track density in the external detector over the dosimeter glass.

Upper Devonian-Mesozoic stratigraphy exposed at the surface and the basal decollement. Subsurface data provide some constraint for the easternmost structures of the SA at this latitude, but the coverage is not as extensive or well resolved as the data constraining SA structure at 19.5°S (compare *Dunn et al*. [1995] to *Moretti et al*. [1996]). To explore the sensitivity of the SA shortening magnitude to stratigraphic thickness variations, we calculate a range of possible SA shortening magnitudes based on the documented thickness range of the Silurian-Devonian section (3–4 km) [*Dunn et al*., 1995; *McQuarrie*, 2002; *Moretti et al*., 1996]. However, these estimates may not reflect kinematically viable shortening magnitudes unless demonstrated in a balanced cross section. SA structures involving Silurian through Mesozoic strata in Figure 2 have an area of 1559 km^2 and thickness of 7 km. Area balance calculations [*Namson and Mitra*, 1989] estimate 86 km of SA shortening based on these values. Reducing the thickness of the Silurian-Devonian duplexes from 3.5 to 3 km results in 123 km of SA shortening, a 37 km increase. If the duplexes are as thick as 4 km, SA shortening decreases by 29 to 57 km.

[39] Alternatively, hanging wall cutoffs projected beyond the erosion surface could represent additional shortening that inflates the overall shortening estimate. In the SA, two major thrusts are projected >3 km above the erosion surface for a total length of 15 km (Figure 2). Greater eroded hanging wall bed lengths are also possible, suggesting a 71–101 km range of possible SA shortening (86 ± 15 km, 17% uncertainty) assuming a Gaussian uncertainty distribution [after *Judge and Allmendinger*, 2011]. Across the entire fold-thrust belt, 45 km of total bed length is projected above the erosion surface in unconstrained hanging walls, suggesting a possible lower bound of 220 km shortening versus 265 km determined from the cross section (17% difference, Figure 2).

[40] To discuss the kinematic implications for the 123, 101, 71, and 57 km shortening scenarios described above, we assume that SA shortening must be balanced by lower basement thrust slip and that the Toro Toro syncline accurately constrains the location of the lower basement thrust footwall ramp [*Allmendinger and Zapata*, 2000; *Kley*, 1996; *McQuarrie*, 2002]. Consequently, each of the SA shortening estimates implies different basement thrust hanging wall cutoff locations (Figure 2, letters A, B, C, and D on cross section). Point A represents the eastern limit of the basement thrust for 123 km of SA shortening. This position is not supported by mapping, which requires the IA-SA boundary to be west of the Tertiary basin at San Isidro (Figure 2). Point B (101 km SA shortening) is ~3 km east of the IA-SA boundary but would require a slightly steeper

Table 2. (U-Th)/He Data

	Sample	ID	Long	Lat	Elev. (m)	Fm Age	^{4}He (mol)	^{238}U (mol)	^{235}U (mol)	^{232}Th (mol)	Raw Age (Ma)	Ft	Corrected Age (Ma)	Age (Ma)	SD. (Ma)
Apatite	10BL19A-1	SA3	−64.05	−17.99	1178	Du	4.92E−16	4.97E−14	3.68E−16	1.20E−13	4.72	0.662	7.13	7.52	0.96
	10BL19A-2						1.56E−15	2.83E−13	2.09E−15	1.88E−14	4.19	0.614	6.82		
	10BL19A-4						1.40E−15	1.30E−13	9.64E−16	2.78E−13	5.59	0.648	8.62		
	10BL19A-3						7.03E−16	3.07E−14	2.27E−16	5.32E−14	12.20	0.601	20.28	[a]	
Zircon	10BL19-1	SA3	−64.05	−17.99	1178	Du	2.05E−12	3.75E−12	2.77E−14	1.63E−12	372.09	0.762	483.5	Not reset	--
	10BL19-2						1.87E−12	3.41E−12	2.52E−14	1.93E−12	364.66	0.764	472.8		
	10BL19-3						2.90E−12	5.19E−12	3.84E−14	3.16E−12	368.55	0.778	469.6		
	10BL22-1	SA1	−63.55	−18.18	684	Du	8.97E−12	1.44E−11	1.06E−13	2.53E−11	336.30	0.847	395.3	Not reset	--
	10BL22-2						8.62E−12	1.61E−11	1.19E−13	5.73E−12	372.04	0.842	439.2		
	10BL22-3						1.12E−12	1.66E−12	1.23E−14	9.07E−13	446.60	0.818	541.5		

[a]Anomalously old age. Replicate age is >50% older than the mean of the other three or more replicates and shows excess helium compared to other replicates with similar U and Th values. This is most likely due to undissolved inclusions of more retentive phases or helium implantation from neighboring phases. Age excluded from calculation of mean age and standard deviation.

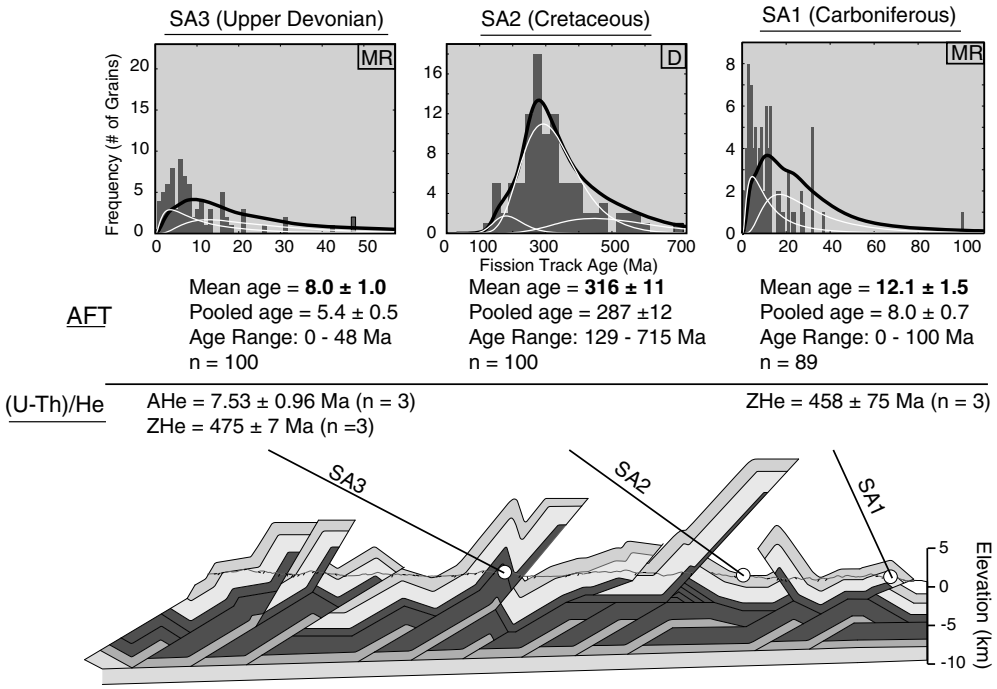

Figure 4. Sub-Andes thermochronology data at the orocline core. AFT grain age distributions for sub-Andean samples are plotted at the top (age of deposition in parentheses). Samples are classified as detrital (D) or mixed-reset (MR) based on *Brandon et al.*'s [1998] criteria. The bold black line is the probability density function for each age distribution, and the fine white lines are component age populations determined with BinomFit [*Brandon et al.*, 1998]. Mean age (±1σ) is calculated from all individual FT grain ages, and the pooled age is based on the track ratio of all the sampled grains. Age range is the oldest and youngest individual grain cooling ages. *n* is the number of grains analyzed for each sample. Ages in bold are those used for interpretation. If available, AHe (apatite (U-Th)/He) and ZHe (zircon (U-Th)/He) ages are listed below AFT data. Uncertainties are 2σ.

basal decollement dip to accommodate both the 10 km thick basement thrust sheet and 8 km of cover stratigraphy below the erosion surface at the Mesozoic-cored synclines near Peña Colorado (Figure 2). A steeper decollement dip would increase the area between the erosion surface and basement thrust, resulting in a larger IA shortening estimate. Points C (71 km shortening) and D (57 km shortening) are not prohibited by the surface geology, but substantial duplexing of Silurian-Mesozoic stratigraphy would be required to fill the space between the basal decollement and the deeper stratigraphic levels exposed at the surface, increasing SA shortening estimates for points C and D, indicating they are not true minima. In general, the area balance error estimates for SA shortening overpredict the error magnitude and cannot be represented by a kinematically viable and geologically accurate cross section. As a result, we prefer 86 ± 15 km SA shortening (points B and C from eroded hanging wall uncertainty) since this shortening range is most consistent with the mapped geology.

4.3. Thermochronology Results

4.3.1. Overview

[41] We report new cooling ages to establish the timing of exhumation and deformation in the orocline axis and constrain the map view reconstruction (Figure 3, Table 1). All AFT cooling ages (apart from EC3) are discordant, so we used central ages in our cooling history interpretations. Reset ages from Carboniferous through Ordovician stratigraphy range from 41 to 8 Ma, and the only unreset age is from Upper Cretaceous strata in the SA (SA2, 316 Ma). We also analyzed two ZHe ages and one AHe age from Upper Devonian and Carboniferous sandstone in the SA (Figure 3, Table 2). Both ZHe ages are detrital, and the AHe age is reset. Overall, ages from all systems indicate that cooling began in

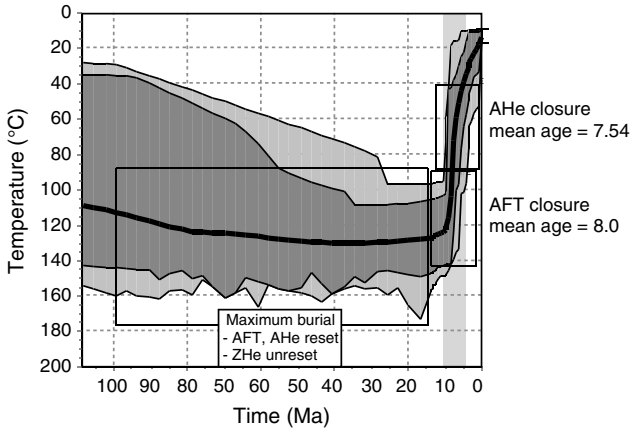

Figure 5. Thermal modeling results for sample SA3 in the sub-Andes. Temperature-time constraints are shown as black boxes. Light-shaded envelope includes acceptable fit cooling histories and dark-shaded region includes good fit thermal histories. Initial rapid cooling 10–5 Ma is highlighted by a vertical grey bar.

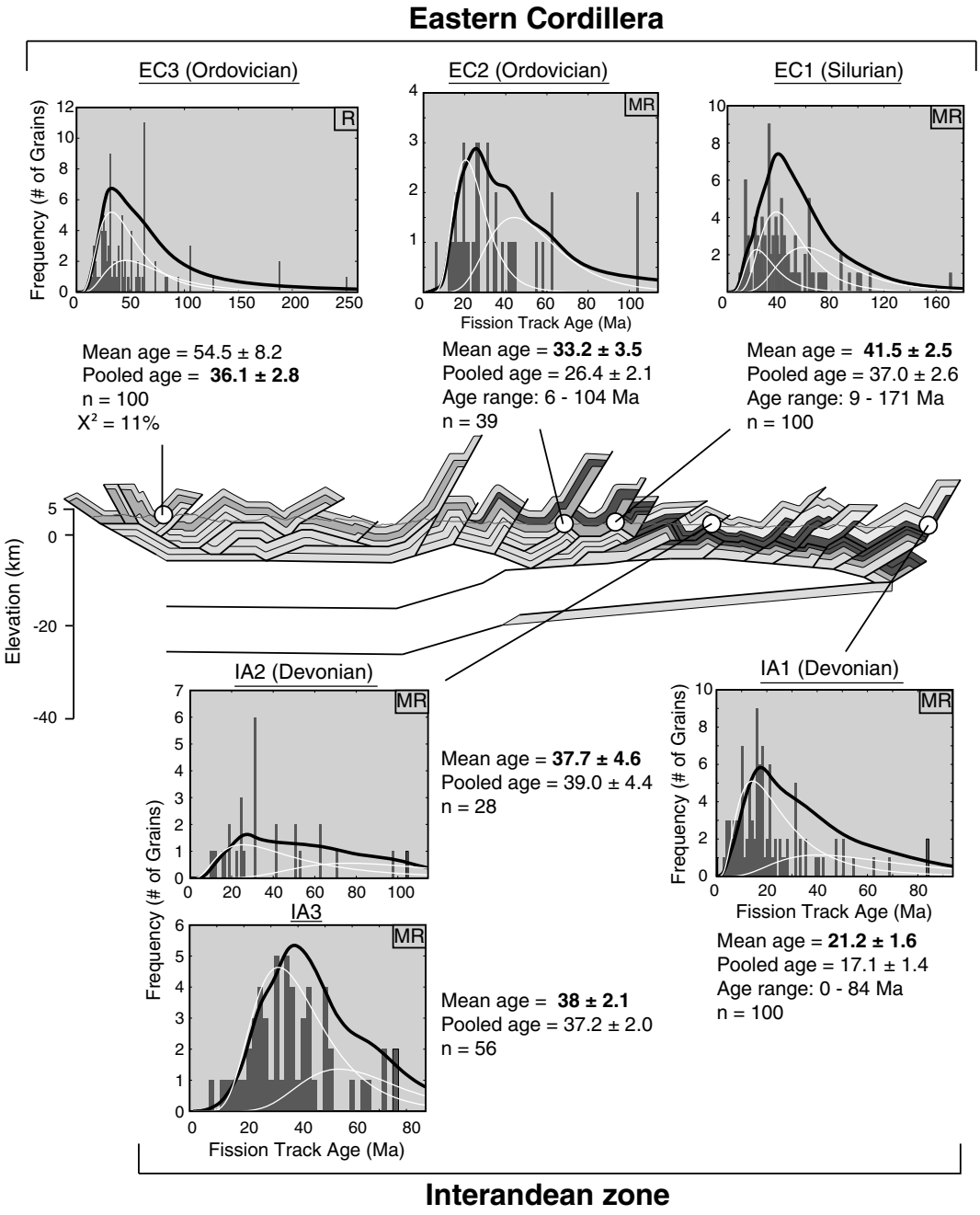

Figure 6. Thermochronology results for the Eastern Cordillera above the cross-section segment and inter-Andean samples below. AFT grain age distributions are formatted as in Figure 5. Sample EC3 at the upper left is classified as reset (R) as it passes the χ^2 test with all grain ages younger than deposition. All others are mixed-reset (MR). (U-Th)/He analyses were not possible for samples from these regions.

the mid-Eocene and progressed eastward through time. We detail individual cooling ages (±1σ) from each structural zone from east to west in the following sections.

4.3.2. Sub-Andes Exhumation

[42] SA samples were collected from the easternmost SA structure (SA1) as well as the shallowest (SA2) and deepest (SA3) SA stratigraphy exposed (Figure 4). SA1 was collected from Carboniferous strata and has a mixed-reset AFT age of 12.1 ± 1.5 Ma (Table 1) and a detrital ZHe age of 459 ± 75 Ma (Table 2). SA2 is from the Upper Cretaceous and has a mean AFT age of 316 ± 11 Ma (Table 1). SA3 is Upper Devonian and has a reset AHe age of 7.5 ± 1.0 Ma (Table 1), a mixed-reset AFT age of 8.0 ± 1.0 Ma, and unreset ZHe ages that range from 395 to 541 Ma (Table 2). Thermal modeling of sample SA3 suggests that rapid cooling began at 10–5 Ma with good fits refining this to 10–7 Ma (Figure 5).

[43] These data collectively constrain the minimum onset of SA cooling to be between 14 and 7 Ma (±1σ) with rapid cooling indicated for an individual structure between 10 and 5 Ma. Detrital ZHe ages indicate that cooling during SA deformation was limited to temperatures below 160°C. Likewise, a detrital Paleozoic AFT age from Upper Cretaceous strata

Table 3a. Orocline Core Exhumation Magnitudes at 18.5°S[a]

Orocline Core	AHe (km)	AFT (km)	ZHe (km)
Sub-Andes	**2.3 (2.1–2.6)**	**4.2 (3.8–4.7)**	7.7 (6.9–8.5)
Inter-Andean zone	2.3 (1.8–3.1)	**3.9 (3.1–5.4)**	6.8 (5.3–9.4)
Eastern Cordillera	2.5 (1.9–3.4)	**4.1 (3.2–5.7)**	7.0 (5.5–9.7)

[a]Magnitudes in bold are calculated from reset cooling ages.

indicates that they were not buried to depths where temperatures exceeded 100°C throughout the Cenozoic.

4.3.3. Inter-Andean Zone Exhumation

[44] We report three discordant AFT cooling ages from the IA: one from the IA-SA boundary (IA1) and two replicate ages (IA2, IA3) from a thrust sheet east of the IA-EC boundary (Table 1, Figure 6). Sample IA1 is from Upper Devonian strata with a mixed-reset age of 21.2 ± 1.6 Ma. Sample IA3 was collected in 2009, resampled (IA2) in 2010, and has mixed-reset ages of 38 ± 2.1 Ma and 37.7 ± 4.6 Ma, respectively. Collectively, these data indicate that rapid cooling initiated in the western IA by ~40 Ma, continuing until at least ~20 Ma at the eastern edge.

4.3.4. Eastern Cordillera Exhumation

[45] The EC samples were taken at the hanging wall of the EC-IA boundary fault (EC1), north of the RNF (EC2), and at the EC forethrust-back thrust transition (EC3) (Table 1, Figure 6). EC1 is from Silurian strata and has a mixed-reset age of 41.5 ± 2.5 Ma. EC2 is from Upper Ordovician strata and yielded a mixed-reset age of 33.2 ± 3.5 Ma. EC3 is from the same stratigraphic level and has a concordant, reset pooled age of 36.1 ± 2.8 Ma. Overall cooling of the EC initiated by ~44 Ma and continued until at least ~30 Ma which mostly overlaps with cooling in the IA.

5. Discussion

5.1. Deformation at the Orocline Core

5.1.1. Sub-Andes Deformation

[46] SA cooling ages at the orocline core range from 15 to 6 Ma within 2σ uncertainty (Figure 4) with a thermal model indicating that rapid cooling began 10–5 Ma (SA3, Figure 5). Sample SA1 from the easternmost SA structure records cooling through AFT-sensitive temperatures by 9 Ma (SA1). This implies that out-of-sequence deformation may have taken place during faulting of the axial SA [see also *Moretti et al*., 1996]; however, we cannot differentiate between specific ages on individual thrusts. Based on the kinematics from the cross section, these cooling ages indicate that the lower basement was active and driving SA deformation by ~15 Ma.

5.1.2. Eastern Cordillera and Inter-Andean Zone Deformation

[47] EC AFT cooling ages indicate cooling by 46–26 Ma, overlapping with 48–28 Ma IA cooling near the EC-IA boundary (IA2, IA3). Cooling recorded at the IA-SA boundary is significantly younger (24–18 Ma, IA1) (Figure 6), implying that deformation progressed in sequence from the EC-IA boundary to the IA-SA boundary by ~18 Ma (Figure 3). The overlap in AFT cooling ages from the EC-IA boundary indicates distributed EC-IA deformation since at least ~37 Ma (EC1) and continuing until at least ~26 Ma (EC2) (Figure 6). If deformation of the EC and IA is the result of motion on the upper basement thrust, it must have initiated by 46 Ma and continued to slip until ~18 Ma.

[48] Synorogenic sediments in the Incapampa syncline at 19.5°S suggest a transition from a foredeep to intermontane basin setting at 25–19 Ma, indicating cessation of EC deformation in the southern limb by that time [*Horton*, 2005]. If the same transition is valid for the Toro Toro syncline, the >26 Ma cooling ages in the adjacent EC and IA would suggest that the region surrounding the Toro Toro had undergone deformation just prior to 26 Ma and that the syncline was structurally separated from the foreland by 25 Ma (Figure 6).

5.2. Exhumation at the Orocline Core

[49] A basic observation from the orocline core map pattern is that the depth of stratigraphic exposure increases from the south limb to deeper levels in the orocline core. This correlates with higher shortening estimates for the SA and may be indicative of out-of-plane shortening related to translational displacement in the IA and EC. We test this inference by comparing magnitudes of exhumation in the southern limb and orocline core. We focus on comparing exhumation between the orocline core and southern limb where translational faulting has been documented (Figure 2) and orographic precipitation gradients have been minor compared to the northern limb [*Barnes et al*., 2012].

[50] We calculate the magnitude of exhumation from nominal T_c of each thermochronometer (70°C for AHe [*Farley*, 2002], 110°C for AFT [*Gallagher et al*., 1998], and 180°C for ZHe [*Reiners et al*., 2004]), the local geothermal gradient, and the average surface temperatures for each zone (23°C for the SA, 15°C for the IA, and 10°C for the EC [*Springer and Forster*, 1998; *Instituto Geografico Militar*, 2000; after *Barnes et al*., 2008]. A mean EC geothermal gradient of 24 ± 7°C/km was determined from four western EC boreholes within one crustal thickness distance of the transect (Catavi, Bolivar, Huanuni, and Santa Fe) (data from *Uyeda and Watanabe* [1982] and *Henry and Pollack* [1988]). We assume the same gradient for the IA [after *Barnes et al*.,

Table 3b. Central Andean Exhumation Magnitudes

		Exhumation Magnitude (km)			
Central Andes Exhumation	Latitude	SA	IA	EC	Total
		SA	IA	EC	Total
Barnes et al. [2006] and *McQuarrie et al*. [2008]	15°S–17°S	3.0– < 7.0	4.0–5.0	5.5–7.5[a]	12.5–17.5
Barnes et al. [2012]	17°S–18°S	>3.0–6.0	>3.5–5.9	>3.5–5.10	
This study	18.5°S	3.8–6.9	> 3.1–5.4	> 3.2–5.7	> 10.1–18
Barnes et al. [2008]	19.5°S	<3.8–7.0	2.6–6.5	2.6–6.5	9.0–20.0

[a]Valid for 45 to 25 Ma (exhumation from 45 to 0 Ma is 9–11km and includes exhumation not related to deformation after 15 Ma).

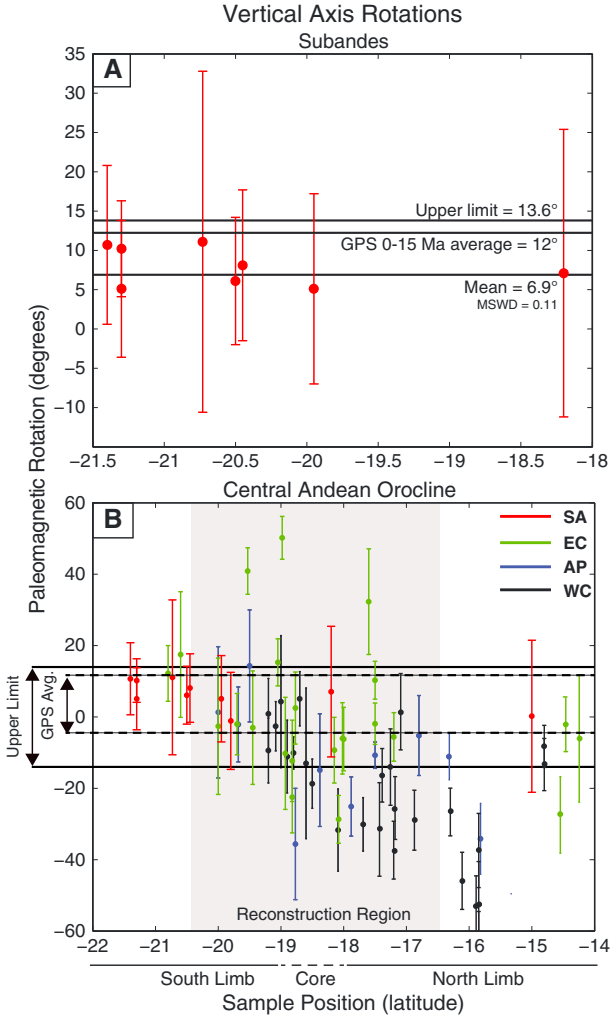

Figure 7. (a) Paleomagnetic rotations from the Bolivian sub-Andes of the orocline [*Roperch et al.*, 2006].Upper bar: The maximum rotation scenario (13.6°) was chosen based on the largest clockwise rotation (for the southern limb) that fell within the uncertainty envelope for all available sub-Andean rotations. Middle bar: Extrapolated GPS rotation rates suggest 12° of southern limb rotation over the 0–15 Ma SA deformation period [*Allmendinger et al.*, 2005]. Lower bar: The mean sub-Andean rotation of 6.9° clockwise was used for the minimum rotation scenario. (b) Paleomagnetic rotations from the sub-Andes (SA), Eastern Cordillera (EC), Altiplano (AP), and Western Cordillera (WC) adjacent to the orocline core [*Arriagada et al.*, 2006; *Roperch et al.*, 2006, 2011]. Bars at ±14° (upper limit) show the envelope of paleomagnetic rotations accounted for in the maximum rotation reconstruction scenario. Dashed lines (GPS avg) show 12° rotation in the southern limb and −4° rotation in the northern limb based on initial SA exhumation and deformation periods [*Allmendinger et al.*, 2005]. Grey band represents latitudes covered by the map view reconstruction model in Figure 8.

2008] because no data exist for the area. Based on this gradient, reset EC and IA AFT ages indicate a minimum of 4.1 km of exhumation (3.2–5.7 within geothermal gradient uncertainty) (Tables 3a and 3b). The mean SA geothermal gradient of 21 ± 2°C/km (from two boreholes, Caranda and Colpa) [*Henry and Pollack*, 1988] and reset AFT ages constrain minimum exhumation to be 4.2 km (3.8–4.7 km). Unreset ZHe ages indicate that SA rocks have not reached temperatures >180°C during the Cenozoic, capping exhumation at 7.7 km (6.9–8.5 km). Thus, a conservative SA exhumation estimate would be 3.8–6.9 km.

5.2.1. Comparison of Orocline Core and Southern Limb

[51] The same geothermal gradients were used for the EC and IA here and in the southern limb [*Barnes et al.*, 2008]. As a result, the exhumation estimates are equivalent, consistent with the similar level of stratigraphic exposure along strike in the EC. For the IA, exhumation in the south limb is estimated to be at least 2.6–6.5 km but less than 6–5 km [*Barnes et al.*, 2008], coinciding with the minimum 3.1–5.4 km of exhumation at the core IA. The SA at 19.5°S has experienced ~5 km of exhumation at most [*Barnes et al.*, 2008] suggesting ~3 km (1–5 km) more exhumation in the SA at the core. This mean 3 km exhumation difference is equivalent to the thickness of SA Tertiary synorogenic sediments at 19.5°S that are absent in SA at 18°S. However, since the Carboniferous and Mesozoic strata are thicker at the core and the geothermal gradient is higher, the increase in exhumation may not solely be the result of Tertiary strata removal. Hydrocarbon maturity data from Upper Devonian strata at the orocline axis indicate that only 2 km of Tertiary burial occurred at 18°S [*Moretti et al.*, 1996], suggesting locally limited preservation of synorogenic sediment. 3-D flexural models based on geoid anomalies of the Andes show decreased distance between the mountain front and forebulge at the axis [*Chase et al.*, 2009], implying less foreland accommodation space compared to the limbs. Regardless, greater SA exhumation at the axis correlates with the higher shortening estimate and deeper stratigraphic exposure relative to the southern limb. The relative increase in deformation at the axial SA since ~18 Ma may be related to the accommodation of limb rotation as the orocline developed.

5.3. Reconstruction of the Orocline Core

[52] Geologic mapping, balanced cross sections, and thermochronology from 16.5°S to 19.5°S provide observations that constrain the age, magnitude, and geometry of fault displacement, sufficient to examine orocline axis kinematics. A map view reconstruction of the orocline core makes it possible to model the observed translational displacements (RNF, Figure 2), account for variable fault displacement directions (Figure 2), and restore vertical axis rotation (Figure 7). The goal of the reconstruction is to estimate the minimum magnitude of out-of-plane deformation required to accommodate orocline deformation and the degree to which it depends on vertical axis rotations. The resolution of the reconstruction is coarse to simplify the model geometry and focus on estimating the magnitude of translational displacement on the RNF system.

5.3.1. Simplified Map View Restoration

[53] The map view reconstruction is composed of polygons based on the map extent of the physiographic zones and subdivided by structural orientation (EC, IA, and SA, Figure 8a). The reconstruction is centered on the orocline core and bounded to the north and south by the map transects of *McQuarrie* [2002] (dashed lines in Figure 8a). We imposed polygon boundaries perpendicular to strike to allow

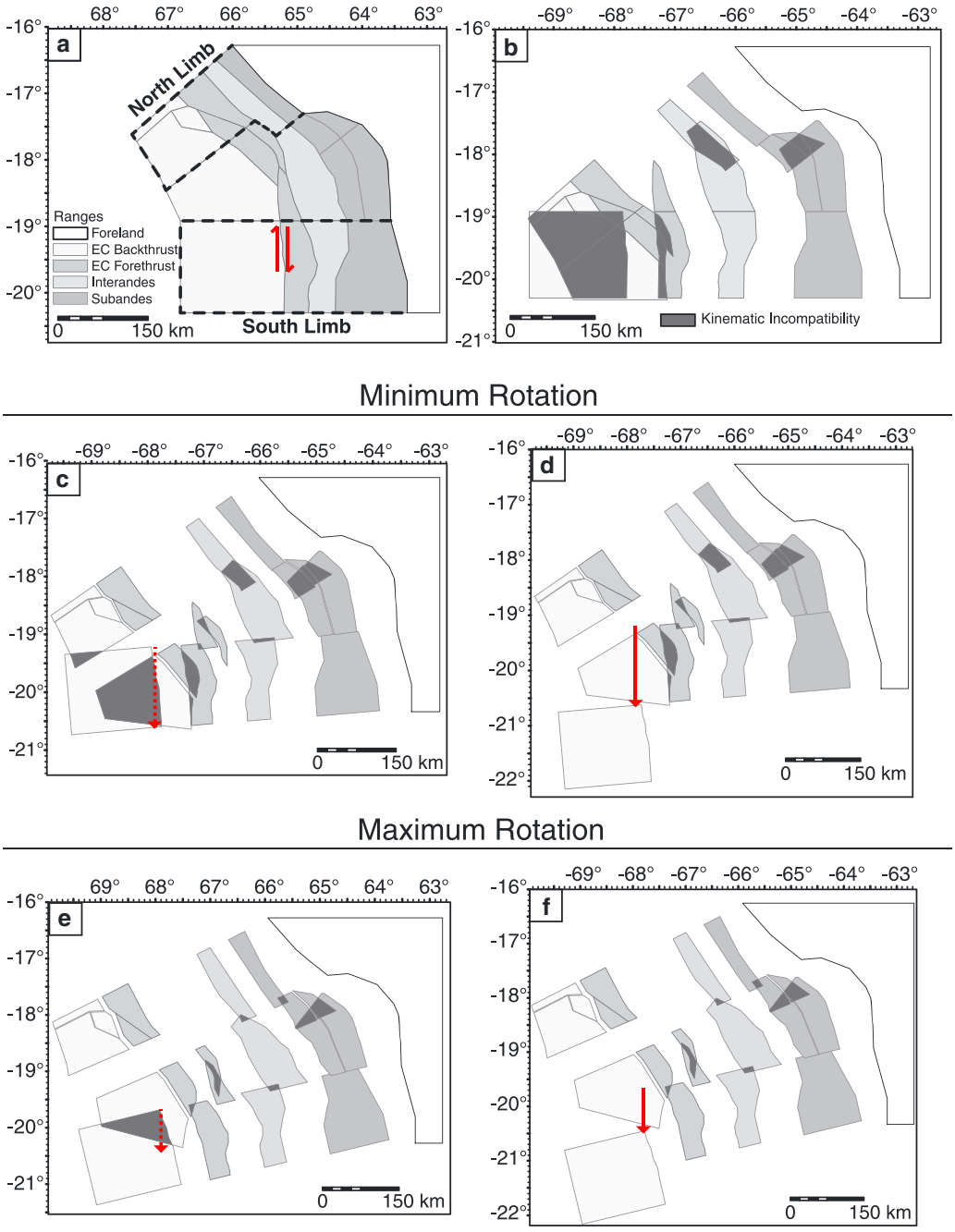

Figure 8. Simplified reconstruction of the Bolivian orocline axis with the addition of new kinematic data from the orocline core. (a) Initial (deformed) model geometry. Fault blocks are defined based on physiotectonic units; internal subdivisions are used to reflect changes in structural orientation and displacement direction. Dashed boxes outline polygons that are restored based on shortening estimates from *McQuarrie* [2002] and timing from *Barnes et al*. [2008] (south limb) and *Barnes et al*. [2012] (north limb). The region of out-of-plane motion determined from mapping is indicated by arrows indicating dextral translation. (b) Restored model geometry with plane strain shortening estimates only (no vertical axis rotations or out-of-plane fault displacements). The resulting kinematic incompatibilities are shown in dark grey for comparison against subsequent restorations that include out-of-plane strain. The area of kinematic inconsistency reflects the lack of kinematic accuracy of each model. Results are summarized in Table 4. (c) Minimum rotation scenario restoring 6.9° of rotation to the limbs. Dashed red arrow indicates overlap resolved by 150 km of out-of-plane displacement. (d) Restoration including minimum out-of-plane translational displacement required to eliminate overlap between the polygons representing the Eastern Cordillera back thrust, indicated by a solid red arrow (150 km). (e) Same as Figure 8c but utilizing 13.6° of rotation. Dashed red arrow indicates overlap resolved by 85 km of out-of-plane displacement. (f) Same as Figure 8e but inferred magnitude of out-of-plane translation is 85 km, indicated by a solid red arrow.

Table 4. Orocline Core Reconstruction Results

	Kinematic Inconsistency (km^2)		
	No Rotation	Minimum Rotation	Maximum Rotation
Sub-Andes	2,446	2,609	1,843
Inter-Andes	2,919	1,884	321
Eastern Cordillera	2,295	1,853	1,186
Eastern Cordillera back thrust	20,448	11,525	4,603
Total	28,108	17,871	7,953
Required translation displacement (km)		150	85
Residual overlap (km^2)		6,346	3,350

the limb and core polygons to move independently based on the kinematics from each transect. Polygon centroid positions were calculated and then displaced by an input vector using a Visual Basic for Applications script in ArcGIS [after *McQuarrie and Wernicke*, 2005]. The reconstruction vectors are defined by displacement magnitudes from shortening estimates, and the displacement direction is assumed to be normal to the mapped fault orientations within a polygon. The magnitude of displacement is restored sequentially based on the relative order of deformation and exhumation for each physiographic unit. More recent SA deformation is restored first, followed by the IA, and finishes with the earliest EC deformation [see *Barnes and Ehlers*, 2009, and references therein]. Since the focus of the model is to estimate the possible range of translational displacement on the RNF, we make the major simplifying assumption that internal strain is negligible and the fault blocks are rigid. In the final restored state, overlapping polygons indicate kinematic incompatibilities where the assigned displacement vector is inaccurate. In Figure 8b, the concentration of overlap ($>20{,}000\,km^2$, red area) in the EC back thrust highlights the localization of incompatibilities when using plane strain shortening estimates alone (similar to Figure 1d). We use the total overlap from this model as the benchmark for the improvement in kinematic accuracy in subsequent models that allow for rotation and translation (Table 4).

[54] Vertical axis rotations for the model area are taken from the paleomagnetic database of *Roeperch et al*. [2006]. Since the restoration is sequential, removal of shortening and rotations is propagated from polygons in the SA (recent deformation) back toward the EC (earlier deformation). No additional rotation is required if SA rotations account for measured EC rotations. For the southern limb SA between 21.5°S and 18°S, nine samples have vertical axis rotations that range in magnitude from $-1.1°$ (counterclockwise) to 11.1° (clockwise) (Figure 7a). Two SA data points are available for the northern limb, recording $0.2 \pm 21°$ at 15°S and $-7.4 \pm 7.2°$ at 12.7°S. These measurements are statistically equivalent, but within the context of the CARP, we assume that $-7.4 \pm 7.2°$ is consistent with orocline-scale deformation and complimentary to south limb rotation. Paleomagnetic data are sparse at the orocline core, so EC rotation direction is assigned based on the structural orientation of each block. Blocks defined by NW-SE structural trends rotated with the northern limb, and N-S trending blocks rotated with the southern limb.

[55] Due to the wide range of possible rotation magnitudes stemming from measurement uncertainties and rotations influenced by local structures, we performed two end-member reconstructions (minimum rotation and maximum rotation) to define the possible envelope of out-of-plane displacement magnitudes. The first model investigates the effect of minimal rotation on modeled translation by restoring only the mean SA rotation (~7°, Figure 7a). The second model uses the maximum permissible rotation within uncertainty of the paleomagnetic data in the reconstruction area. The maximum permissible rotation for the SA in the southern limb is 13.6° and $-14.6°$ in the north limb (Figure 7b). The 7° and 14° rotation end-members encapsulate the range of 10 Myr timescale averaged back-arc rotations from GPS data (8°/10 Myr in the south limb and $-4°$/10 Myr in the north limb) [*Allmendinger et al*., 2005]. This 10 Ma period encompasses the age range of northern SA exhumation and deformation [*Barnes et al*., 2012]; however, exhumation and deformation in the southern limb SA extend over a longer window of 15–0 Ma [*Barnes et al*., 2008]. GPS rotations projected over this window in the southern SA suggest at least 12° of rotation. If these rotation rates were constant throughout EC-SA deformation, total rotation in the EC and IA could be higher due to a longer deformation period. However, in the reconstruction region, most EC paleomagnetic rotations are $<20°$ and only four exceed 14° within uncertainty (Figure 7b). As a result, we feel that a 14° maximum rotation end-member model is sufficient to represent the upper limit of reasonable limb rotation.

5.3.2. Restoration Models

[56] The minimum rotation model ends in a restored state with $17{,}939\,km^2$ of total overlap, $11{,}525\,km^2$ of which is focused in the EC back thrust (Figure 8c, Table 4). Allowing 150 km of N-S translational displacement on the RNF (indicated by red arrows in Figures 8c and 8d) eliminates all but $6414\,km^2$ of residual overlap in the EC, IA, and SA (Figure 8d). This solution reduces overlap by 77% from Figure 8b but requires substantial translational displacement on the RNF. A secondary concentration of overlaps ($>1000\,km^2$) is observed in the EC forethrust, IA, and SA where the structural orientation gradually changes from NW-SE to N-S. These overlaps are due to the coarse scale of this reconstruction, which groups these structures into semiarbitrary polygons.

[57] By increasing the magnitude rotation to ~14°, total overlap in the maximum rotation model drops to $7473\,km^2$ (Figure 8e, 73% reduction from Figure 8b). Larger vertical axis rotations reduce overlap between the orocline core and the northern limb but have less of an effect on the core and southern limb (compare Figures 8e and 8d). Strain incompatibility is still localized in the EC back thrust although the overlap is reduced by ~$20{,}000\,km^2$ (Table 4). The EC back thrust overlap is resolved by imposing 85 km of N-S translational motion along the RNF (red arrow, Figures 8e and 8f). This eliminates $4603\,km^2$ of overlap, leaving $2870\,km^2$ of residual overlap distributed across the fold-thrust belt (Table 4, Figure 8f) for a 90% reduction of overlap area (compare Figures 8b and 8f). Areas of strain incompatibility persist in the SA and IA, but the total overlap is reduced. Overlap in the IA and EC forethrust of the core and north limb is reduced to 321 and $706\,km^2$, respectively. The SA sees less of an improvement, indicating that rotation alone will not resolve the inconsistency.

[58] In both cases, the northern limb has minimal overlap with the core region, except where noted in the IA and SA. In terms of constraining the magnitude of N-S translation

based on resolving overlap west of the RNF, the result is more sensitive to the magnitude rotation in the southern limb than the northern limb. In the southern limb, 14° of rotation (Figures 8e and 8f) is consistent with time-averaged GPS rotations but is 4° greater than the averaged GPS rotation for the northern limb thrust belt [*Allmendinger et al*., 2005]. Allowing 8° of rotation in the northern limb and 14° of rotation on the southern limb results in 12,500 km^2 of overlap and predicts 98 km of N-S translational motion on the RNF, 13 km more than the maximum rotation model estimate.

[59] The magnitude of overlap and estimated out-of-plane displacement is even less sensitive to potential shortening uncertainties in the orocline core and southern limb. We investigated the sensitivity of the translation estimate to SA shortening estimates of 64 ± 17 km in the southern limb [*Judge and Allmendinger*, 2011] and 86 ± 15 km in the core. With 101 km of SA shortening at the orocline core (Figure 2, point B) and 81 km of shortening in the southern limb SA, estimated RNF translation is 85 km. If SA shortening is reduced to 71 km at the core (Figure 2, point C) and 47 km in the southern limb, translation on the RNF is estimated to be 81 km. In the minimum rotation model (Figures 8c and 8d), upper (point B) and lower bound (point C) shortening estimates predict 174 km of translation and 150 km, respectively. Overall, the effect of SA shortening uncertainty on RNF displacement estimates is minor. Estimated translation is most sensitive to limb rotation because rotation directly alters the orientation of the limb displacement paths. In the minimum rotation model, displacement paths trend to 237° in the northern limb and 266° in the southern limb. However, in the maximum rotation model, the limb displacement path trends only differ by 12° (245° in the northern limb and 257° in the southern limb, Figures 8c–8f) compared to 29° in the minimum rotation model. Greater limb rotation results in increasingly parallel displacement paths, reducing both strain incompatibility and the magnitude of translation estimated to resolve the remaining overlap.

5.4. Implications for Orocline Formation

[60] We can relate overlap in the map view reconstructions to specific kinematic deficiencies such as the lack of translational displacement or rotation. Our restorations show that minor overlap (<600 km^2) initially appears in the EC back thrust belt by ~5–8 Ma after roughly half of SA shortening (~30–40 km) and rotation has been restored. Removal of this overlap via motion on the RNF implies that translation along the RNF continued after the main phase of EC deformation and exhumation (~20 Ma) [*Barnes et al*., 2008; this study]. However, most of the overlap (~4600 km^2; maximum rotation scenario) occurs in the region of the EC back thrust zone and is most apparent after EC deformation (20–45 Ma) is removed. Therefore, strike-slip displacement probably initiated prior to 20 Ma.

[61] Timing of strike-slip motion is the same for both reconstructions because it is dependent on EC deformation (>20 Ma) rather than rotation within the SA (<20 Ma). As shown above, larger limb rotations result in more parallel shortening directions for both limbs. In the reconstruction, larger rotations reduce both the total block overlap and, ultimately, the magnitude of translation required to resolve that overlap. We prefer the maximum rotation scenario because the rotation magnitude is within the paleomagnetic data uncertainty across the width of the central Andes from 10°S to 30°S and is consistent with time-averaged GPS rotations (Figure 7) [*Allmendinger et al*., 2005; *Arriagada et al*., 2006; *Roperch et al*., 2006; *Taylor et al*., 2005, 2007]. A minimum estimate of translation in the RNF is critical because translation along the fault requires north directed shortening and an additional component in crustal thickening. Assuming that northward displacement on the western side of the RNF is accommodated by equivalent shortening on NW-SE thrust faults, 150 km of north directed displacement would require more N-S shortening than the magnitude of E-W shortening accommodated in the EC (136 km, Figure 2). For comparison, the maximum rotation model predicts 85 km of translation, equivalent to the shortening estimate for the SA at the core (86 km). We prefer the maximum rotation model because the out-of-plane shortening magnitude is comparable to the plane strain shortening estimates.

[62] Our preferred reconstruction implies that the central Andean thrust belt was initially less arcuate and had a roughly NNW-SSE trend, comparable to the results of *Arriagada et al*. [2008]. Since curvature increased over time, the central Andean orocline is best classified as a "progressive arc" whereby curvature is progressively developed due to either differential shortening or curved slip paths [*Weil and Sussman*, 2004]. Orogen-wide shortening estimates used for this reconstruction are all similar, but SA shortening at the core (86 km) is 19 km larger than the southern SA (67 km) and 14 km larger than the northern SA (72 km) [*McQuarrie*, 2002]. Within the largest estimates of shortening uncertainty (northern SA: ±27 km, southern SA: ±17 km) [*Judge and Allmendinger*, 2011], these magnitudes would be equivalent. However, the depth of stratigraphic exposure, reset AFT ages, and magnitude of exhumation all argue for greater deformation in the orocline core SA than to the north or south. In Bolivia, differential SA shortening between the limbs and core amounts to rotations of −3° in the northern limb [*McQuarrie et al*., 2008] and 6° in the southern limb [*McQuarrie*, 2002], suggesting that curved slip paths impart a significant component of rotation. The progressive arc model does not account for translational displacements parallel to strike, but our data suggest that they may be necessary in order to accommodate net material convergence toward the orocline axis.

[63] Elastic dislocation models of the 1998 $M_w = 6.6$ Aiquile earthquake indicate that a N-S oriented fault with right-lateral offset best explains the interferometric synthetic aperture radar (InSAR) displacement field [*Funning et al*., 2005] (Figure 2). This fault plane solution is structurally consistent and approximately along strike of the RNF, suggesting that right-lateral faulting has propagated north in recent time. Assuming that local 45–28 Ma AFT ages (EC1 and EC2 in Figure 6) reflect initiation of deformation concurrent with N-S translation and that translation is ongoing today, RNF slip rates of ~2–3 mm/yr and ~3–5 mm/yr are predicted by the maximum and minimum rotation models, respectively. Local east directed GPS velocities for the EC-SA at 18.5°S suggest permanent SA deformation rates of ~9.5 mm/yr [*Bevis et al*., 2001], while long-term shortening rates for SA deformation range from 5.7 to 8.5 mm/yr (86 km over 10–15 Myr). Conservatively, the N-S translational slip rates are approximately a third of the observed GPS velocity, but well-resolved north directed displacements

are not present in current GPS data for the region. This could be due to the lack of GPS station coverage in the RNF/Aiquile earthquake epicentral area. *Lamb* [2000] and *Allmendinger et al*. [2005] have argued that limb rotation is an ongoing process and that oroclinal curvature continues to increase today. If translational displacements are a key mechanism for accommodating limb rotation as suggested by our reconstructions, it would make sense that faults such as the RNF are still active. In turn, this implies that crustal thickening focused at the orocline axis is still occurring either as a slow and steady process that has been active since ~45 Ma [*Barnes and Ehlers*, 2009, and references therein] or as a renewed response to lithospheric delamination [e.g., *Garzione et al*., 2008]. Rapid removal of lower crust/lithosphere is predicted to enhance SA shortening and, as a result, may enhance limb rotation, orocline curvature, and increased thickening of the orocline core.

[64] Orocline kinematics [e.g., *Kley*, 1999; *Arriagada et al*., 2008] and modern GPS rotations [*Allmendinger et al*., 2005] all support displacement paths that converge on the orocline axis and imply orogen-parallel shortening. While this concept has been theoretically explored through numerical models and reconstructions [*Arriagada et al*., 2008; *Boutelier and Oncken*, 2010; *Dewey and Lamb*, 1992; *Hindle et al*., 2005; *Kley*, 1999], this is the first time the mechanisms accommodating orogen-parallel displacement have been physically documented. The local reconstruction presented here has displacement trajectories comparable to prior large-scale reconstructions [e.g., *Arriagada et al*., 2008; *Hindle et al*., 2005]. However, new data from the orocline core show that orogen-parallel shortening occurs mostly between the core and southern limb, as opposed to prior models where it assumed to be symmetric in both limbs [*Kley*, 1999; *Hindle et al*., 2005]. The results of the reconstruction quantify the possible magnitude of orogen-parallel translation that has taken place, a critical consideration for crustal thickening of the Altiplano [e.g., *Hindle et al*., 2005]. By quantifying out-of-plane displacement in the central Andes, we can begin to assess the influence orocline formation may have had on focusing crustal thickening in the Altiplano region and its role in the uplift history of the Andean Plateau.

6. Conclusions

[65] This study presents new mapping, shortening estimates, and cooling histories from the central Andean orocline that characterizes the kinematics, spatiotemporal evolution of deformation and exhumation, and the magnitude of material transport along strike. We provide direct field evidence from the orocline core that documents the location, orientation, and kinematics of structures accommodating strike-parallel transport in the central Andean orocline. We infer substantial along-strike displacement within the orocline core and suggest that it is a key factor in accurately determining the impact of orocline formation on crustal thickening.

[66] Our primary conclusions are as follows:

[67] 1. The orocline core possesses variable structural orientations from N-S in the SA to NW-SE in the EC. The SA structures are oriented N-S, comparable to the southern limb SA. Structural orientation gradually changes across the IA and obliquely intersects the NW-SE trend of EC structures. New mapping at this intersection shows that at least one fault (the Rio Novillero Fault) has accommodated dextral N-S translation in addition to thrust displacement. The location of the fault is in close structural proximity to the 1998 Aiquile $M_w = 6.6$ earthquake, shown by InSAR and modeling to be the result of a N-S oriented right-lateral fault.

[68] 2. Shortening perpendicular to strike at the orocline core in the EC, IA, and SA is ~265 km (40%) for a total of 313 km (36%) including Altiplano shortening [*McQuarrie*, 2002]. This is equivalent to shortening to the north (300 km) but ~30 km less than to the south. Most (60%) of the total shortening in the orocline is accommodated in the EC and IA. The shortening magnitude in the SA is higher (86 km) than in the north (72 km) or south (67 km) and represents a larger proportion of the shortening budget (27%) compared to the north (24%) or south (21%) [*McQuarrie*, 2002]. Based on stratigraphic uncertainties, SA shortening could range from 57 to 123 km, but the map data are most compatible with 86 ± 15 km of shortening.

[69] 3. AFT cooling ages decrease eastward from the EC/IA to the SA within the orocline core. In each zone, cooling ages overlap within uncertainty, suggesting distributed exhumation and deformation. Cooling ages from the EC and IA range from 46 to 18 Ma. AFT cooling ages from the SA span 15–6 Ma, and a single thermal model indicates that rapid cooling began 10–5 Ma. We propose that slip transferred to a lower basement thrust by ~18–15 Ma based on these ages.

[70] 4. Mean exhumation magnitudes increase westward from a maximum of 6.9 km (range 3.8–6.9 km) in the SA to a minimum of 3.2 km (minimum range 3.2–5.7 km) in the EC. The SA in the orocline core has more exhumation compared to the southern limb and at least as much exhumation as the northern limb. This is consistent with a higher magnitude of deformation and lack of broad fault-bounded piggyback basins that preserve Tertiary synorogenic sediment in the core.

[71] 5. Map view reconstruction of the orocline core synthesizes the orocline core kinematics with the adjacent limbs using two end-member rotation models. Our preferred model allows for ±14° of limb rotation estimated from a kinematically viable envelope of paleomagnetic rotation magnitudes and estimates 85 km of translational displacement on the Rio Novillero Fault. If the Aiquile earthquake reflects ongoing translational displacement in the region, long-term slip rates of 2–3 mm/yr are possible based on this model. Translation estimates are most sensitive to changes in rotation between the southern limb and orocline core but less sensitive to variations in SA shortening. Uncertainties in both limb rotation and SA shortening provide RNF translation estimates ranging from 80 to 98 km.

Appendix A: Analytical Procedures

A1. Apatite Fission Track Analysis

[72] Apatite fission track (FT) analysis was carried out in the fission track laboratory at the University of Tübingen. Apatite grains were embedded in epoxy, ground, and polished to expose internal surfaces of the grains. The apatite mounts were etched in 5.5 mol HNO_3 for 20 s at 20°C to reveal the spontaneous tracks that intersect the apatite surface. Afterward, the mounts were covered with a 50 μm thick,

uranium-free muscovite external detector and irradiated with thermal neutrons at the research reactor facility FRM-II in Garching (Germany). We included uranium glass IRMM-540 covered with a muscovite external detector, as dosimeters of the neutron fluence in the irradiation package. After irradiation, the muscovite external detectors were etched in 40% HF for 30 min to reveal the induced fission tracks. After etching, the external detector was placed back to its original position on top of the polished apatite surface for track counting. Spontaneous and induced fission tracks were counted at a nominal magnification of 1000X using a Zeiss AxioImager M2M microscope, by focusing first at the apatite surface and then up into the surface of the external detector [*Jonckheere et al*., 1993]. The zeta age was calculated according to *Hurford* [1990] and using a zeta calibration factor of 245 ± 6 a cm^2 (E. Enkelmann) and 210 ± 11 a cm^2 (A.K. Schatz). The zeta calibration was done by analyzing 14 age standards (Fish Canyon Tuff and Durango) included in two irradiations.

A2. U-Th/He Analysis

[73] Clear and undisturbed apatite grains without inclusions were selected using a binocular microscope. The grain dimensions were measured for the calculation of the alpha-correction factor after *Farley et al*. [1996]. Afterward, the single grains were packed in Nb tubes for U-Th/He analysis. In general, we analyzed three aliquots per sample. The samples were analyzed in the Patterson helium extraction line at the University of Tübingen, which is equipped with a 960 nm diode laser to extract the helium gas. Zircon grains were heated for 5 min at 10 A. Each grain was heated again and analyzed to make sure that the grain was degassed entirely in the first step. The reextracts generally showed $<1\%$ of the first signal. After helium analysis, the grain packages were sent to the University of Arizona at Tucson for U and Th measurements using an ICP-MS. The analytical error of the mass spectrometer measurements is generally very low and does not exceed 2%. In contrast, the reproducibility of the sample age constitutes a much larger error.

A3. Figure 2 Cross-section Annotations

[74] 1. Dip of basement and thickness of foredeep are from industry seismic data [*Dunn et al*., 1995; *Baby et al*., 1995, *Moretti et al*., 1996] and after the cross section by *Moretti et al*. [1996]. 1.5 -2 km thickness of Tertiary syn-orogenic sediment is used based on hydrocarbon maturity data from Moretti *et al*. [1996].

[75] 2. The position of the Mandeyapecua thrust fault system is based on topography in the foredeep assumed to be the product of fault-bend folding at depth. This corresponds with the position of the of the faults as presented by *Moretti et al*. [1996] and *Brooks et al*. [2010].

[76] 3. Thickness of Ordovician and Silurian strata are unknown but considered to be presented based on extent of Paleozoic depositional area [*Sempere*, 1995]. Since the Sub-Andes here are structurally continuous and stratigraphically similar to the south limb, the thicknesses used are similar to the southern section of *McQuarrie* [2002] at 19.5° Sub-Andes at this latitude (e.g. *Moretti et al* [1996]).

[77] 4. Duplexing of Upper Devonian strata used to explain tight anticline and map exposure of tightly deformed upper Devonian shales (after *McQuarrie* [2002]). This fold has a similar geometry and stratigraphy to Sub-Andean anticlines to the south that have been drilled and seismically imaged [*Dunn et al*. 1995]. The length of the hanging wall projected above the erosion surface is equivalent to length of duplexed Upper Devonian strata required to explain the anticline geometry.

[78] 5. Middle Devonian shales are exposed at core of anticline indicating that a horse from below the Upper Devonian detachment breaches the erosion surface.

[79] 6. Eastern limit of lower basement thrust. This position is interpreted based on increase in structural elevation at Interandean - Sub-Andean boundary. This requires involvement of Ordovician strata and basement to fill space between surface and decollemont.

[80] 7. Dip of decollemont increases to 4° [*McQuarrie*, 2002]

[81] 8. Western limit of preserved Carboniferous strata. Westward pinch-out of Carboniferous due to pre-Mesozoic erosion is inferred to begin here due to proximity of Devonian-Cretaceous contact in synclines to the west and along strike to the north. West of the Sub-Andes, the full thickness of Cretaceous strata is only constrained at the Toro-Toro syncline.

[82] 9. Increase in Ordovician strata thickness proposed based on thicknesses exposed in Eastern Cordillera ~20 km to the west and along strike to the north.

[83] 10. Slip on lower basement thrust is limited to shortening accommodated on Sub-Andean structures. Continuation of Ordovician strata below the upper basement thrust is required to balance Sub-Andean shortening.

[84] 11. Western limit of Devonian strata. Cretaceous rocks to the west rest on top of Upper Silurian strata with minor, local preservation of lower Devonian strata.

[85] 12. Stacked basement thrust required to explaine increase in structural elevation and uniform structural elevation to the west (after *McQuarrie* [2002]). Position of upper basement thrust hanging wall cut off constrained by exposure of lower Ordovician shales in high peaks to the west of broad synclines cored by Devonian and Cretaceous strata. Orodivician duplex below Devonian syncline required to explain elevation of syncline floor.

[86] 13. Base of lower basement thrust footwall is below Toro Toro Syncline. The position of basement thrust foot wall is independently corroborated by magnitude of lower basement thrust slip estimated from Sub-Andean shortening. A 20° foot wall ramp was required to explain width of the Toro Toro Syncline.

[87] 14. Duplex of Ordovician rocks required to explain broad exposure of prevaisvely folded lower Ordovician strata. Relatively low elevation of region did not neccesitate involvement of an additional basement thrust.

[88] 15. Position of basement ramp and upper basement thrust foot wall is constrained by along strike position from ramp in the northern section of *McQuarrie* [2002] which was based on seismic reflection data.

[89] The position of the ramp at this location is consistent with the amount of slip on the upper basement thrust required by the magnitude of shortening accommodated in the Eastern Cordillera and Interandean zone.

[90] **Acknowledgments.** We thank SERGEOTECMIN of La Paz, Bolivia for providing land access credentials. Jamie Tito and Sohrab Tawackoli were invaluable as in-country guides and made fieldwork in Bolivia logistically possible. Keegan Runnals, Wes Farnsworth, and Andrew Budnick assisted in field mapping and sample collection. Insightful reviews from Onno Oncken, César Arriagada, and an anonymous reviewer greatly improved the overall quality of the manuscript. Support for this work was provided by NSF grant EAR 0908972.

References

Allmendinger, R. W., and T. R. Zapata (2000), The footwall ramp of the Subandean decollemont, northernmost Argentina, for extended correlation of seismic reflection data, *Tectonophysics*, *321*, 37–55.

Allmendinger, R. W., T. E. Jordan, S. M. Kay, and B. L. Isacks (1997), The evolution of the Altiplano-Puna plateau of the central Andes, *Annu. Rev. Earth Planet. Sci.*, *25*, 139–147.

Allmendinger, R. W., R. Smalley Jr., M. Bevis, H. Caprio, and B. Brooks (2005), Bending the Bolivian orocline in real time, *Geology*, *33*, 905–908, doi:10.1130/G21779.1.

Arriagada, C., P. Roperch, C. Mpodozis, and R. Fernandez (2006), Paleomagnetism and tectonics of the southern Atacama Desert (25–28°S), northern Chile, *Tectonics*, *25*, TC4001, doi:10.1029/2005TC001923.

Arriagada, C., P. Roperch, C. Mpodozis, and P. R. Cobbold (2008), Paleogene building of the Bolivian Orocline: Tectonic restoration of the central Andes in 2-D map view, *Tectonics*, *27*, TC6014, doi:10.1029/2008TC002269.

Baby, P., G. Herail, R. Salinas, and T. Sempere (1992), Geometry and kinematic evolution of passive roof duplexes deduced from cross section balancing: Example from the foreland thrust system of the southern Bolivian Subandean Zone, *Tectonics*, *11*, 523–536, doi:10.1029/91TC03090.

Baby, P., I. Moretti, B. Guillier, R. Limachi, E. Mendez, J. Oller, and M. Specht (1995), Petroleum system of the northern and central Bolivian sub-Andean zone, *AAPG Mem.*, *62*, 445–458.

Barbarand, J., A. Carter, I. Wood, and T. Hurford (2003), Compositional and structural control of fission-track annealing in apatite, *Chem. Geol.*, *198*, 107–137, doi:10.1016/S0009-2541(02)00424-2.

Barke, R., S. H. Lamb, and C. MacNiocaill (2007), Late Cenozoic bending of the Bolivian Andes: New paleomagnetic and kinematic constraints, *J. Geophys. Res.*, *112*, B01101, doi:10.1029/2005JB004372.

Barnes, J. B., and T. A. Ehlers (2009), End member models for Andean Plateau uplift, *Earth Sci. Rev.*, *97*, 117–144, doi:10.1016/j.earscirev.2009.08.003.

Barnes, J. B., and W. A. Heins (2009), Plio-Quaternary sediment budget between thrust belt erosion and foreland deposition in the central Andes, southern Bolivia, *Basin Res.*, 21, 91–109.

Barnes, J. B., T. A. Ehlers, N. McQuarrie, P. B. O'Sullivan, and J. D. Pelletier (2006), Eocene to recent variations in erosion across the central Andean fold-thrust belt, northern Bolivia: Implications for plateau evolution, *Earth Planet. Sci. Lett.*, *248*, 118–133, doi:10.1016/j.epsl.2006.05.018.

Barnes, J. B., T. A. Ehlers, N. McQuarrie, P. B. O'Sullivan, and S. Tawackoli (2008), Thermochronometer record of central Andean Plateau growth, Bolivia (19.5°S), *Tectonics*, *27*, TC3003, doi:10.1029/2007TC002174.

Barnes, J. B., T. A. Ehlers, N. Insel, N. McQuarrie, and C. J. Poulsen (2012), Linking orography, climate, and exhumation across the central Andes, *Geology*, *40*, doi:10.1130/G33229.1.

Beck, M. (2004), The central Andean rotation pattern: Another look, *Geophys. J. Int.*, *157*(3), 1348–1358, doi:10.1111/j.1365-246X.2004.02266.x.

Benjamin, M. T., N. M. Johnson, and C. W. Naeser (1987), Recent rapid uplift in the Bolivian Andes: Evidence from fission-track dating, *Geology*, *15*, 680–683.

Bevis, M., E. Kendrick, R. Smalley Jr., B. Brooks, R., and Allmendinger, B. Isacks (2001), On the strength of interplate coupling and the rate of back arc convergence in the central Andes: An analysis of the interseismic velocity field, *Geochem. Geophys. Geosyst.*, *2*, doi:10.1029/2001GC000198.

Boutelier, D. A., and O. Oncken (2010), Role of the plate margin curvature in the plateau buildup: Consequences for the central Andes, *J. Geophys. Res.*, *115*, B04402, doi:10.1029/2009JB006296.

Boyer, S. E., and D. Elliott (1982), Thrust systems, *AAPG Bull.*, *66*, 1196–1230.

Brandon, M. T. (2002), Decomposition of mixed grain age distributions using BinomFit, *On Track*, *24*, 13–18.

Brandon, M. T., M. K. Roden-Tice, and J. I. Garver (1998), Late Cenozoic exhumation of the Cascadia accretionary wedge in the Olympic Mountains, northwest Washington State, *Geol. Soc. Am. Bull.*, *110*, 985–1009, doi:10.1130/0016-7606.

Brooks, B. A., et al. (2011), Orogenic-wedge deformation and potential for great earthquakes in the central Andean backarc, *Nat. Geosci.*, *4*, 380–383, doi:10.1038/ngeo1143.

Carey, S. W. (1955), The orocline concept in geotectonics - Part I, *Pap. Proc. R. Soc. Tasmania*, *89*, 255–288.

Carlson, W. D., R. A. Donelick, and R. A. Ketcham (1999), Variability of apatite fission-track annealing kinetics: I. Experimental results, *Am. Mineral.*, *84*, 1213–1223.

Chase, C. G., A. J. Sussman, and D. D. Coblentz (2009), Curved Andes: Geoid, forebulge, and flexure, *Lithosphere*, *1*, 358–363, doi:10.1130/L67.1.

Coutand, I., P. Gautier, P. R. Cobbold, M. de Urreiztieta, A. Chauvin, D. Gapais, E. A. Rossello, and O. Lopez-Gammundi (2001), Style and history of Andean deformation, Puna plateau, northwestern Argentina, *Tectonics*, *20*(2), 210–234, doi:10.1029/2000TC900031.

Crowley, K. D., M. Cameron, and R. L. Schaefer (1991), Experimental studies of annealing of etched fission tracks in fluorapatite, *Geochim. Cosmochim. Acta*, *55*, 1449–1465, doi:10.1016/0016-7037(91)90320-5.

Dahlstrom, C. D. A. (1969), Balanced cross sections, *Can. J. Earth Sci.*, *6*, 743–757.

Dewey, J. F., and S. Lamb (1992), Active tectonics of the Andes, *Tectonophysics*, *205*, doi:10.1016/0040-1951(92)90419-7.

Dodson, M. H. (1973), Closure temperature in cooling geochronological and petrological systems, *Contrib. Mineral. Petrol.*, *40*, 259–274.

Donelick, R. A., P. B. O'Sullivan, and R. A. Ketcham (2005), Apatite fission-track analysis, in *Low Temperature Thermochronology: Techniques, Interpretations, and Applications*, edited by P. W. Reiners and T. A. Whlers, *Rev. Mineral. Geochem.*, *58*, 49–94, doi:10.2138/rmg.2005.58.3.

Dunn, J. F., K. G. Hartshorn, and P. W. Hartshorn (1995), Structural styles and hydrocarbon potential of the sub-Andean thrust belt of southern Bolivia, *AAPG Mem.*, *62*, 523–543.

Ege, H., E. R. Sobel, E. Scheuber, and V. Jacobshagen (2007), Exhumation history of the southern Altiplano plateau (southern Bolivia) constrained by apatite fission-track thermochronology, *Tectonics*, *26*, TC1004, doi:10.1029/2005TC001869.

Ehlers, T. A., and K. A. Farley (2003), Apatite (U-Th)/He thermochronometry: Methods and applications to problems in tectonic and surface processes, *Earth Planet. Sci. Lett.*, *206*, 1–14, doi:10.1016/S0012-821X(02)01069-5.

Ehlers, T. A., et al. (2005), Computational tools for low-temperature thermochronometer interpretation, in *Low-Temperature Thermochronology: Techniques, Interpretations, and Applications*, edited by P. W. Reiners and T. A. Ehlers, *Rev. Mineral. Geochem.*, *58*, 589–622, doi:10.2138/rmg.2005.58.2.

Elger, K., O. Oncken, and J. Glodny (2005), Plateau-style accumulation of deformation: Southern Altiplano, *Tectonics*, *24*, TC4020, doi:10.1029/2004TC001675.

England, P. C., and G. Houseman (1989), Extension during continental convergence, with application to the tibetan plateau: *J. Geophys. Res.*, vol 94, p. 17,561–17,579.

Farley, K. A. (2002), (U-Th)/He dating: Techniques, calibrations, and applications, in *Nobel Gas Geochemistry*, edited by P. D. Procelli et al., *Rev. Mineral. Geochem.*, *47*, 819–843, doi:10.2138/rmg.2002.47.18.

Farley, K. A., R. A. Wolf, and L. T. Silver (1996), The effects of long alpha-stopping distances on (U-Th)/He ages, *Geochim. Cosmochim. Acta*, *60*, 4223–4229, doi:10.1016/S0016-7037(96)00193-7.

Funning, G. J., R. M. D. Barke, S. H. Lamb, E. Minaya, B. Parsons, and T. J. Wright (2005), The 1998 Aiquile, Bolivia earthquake: A seismically active fault revealed with InSAR, *Earth Planet. Sci. Lett.*, *232*, 39–49.

Galbraith, R. F. (1981), On statistical models for fission track counts, *J. Int. Assoc. Math. Geol.*, *13*, 471–478.

Gallagher, K., R. Brown, and C. Johnson (1998), Fission track analysis and its applications to geological problems, *Annu. Rev. Earth Planet. Sci.*, *26*, 519–572, doi:10.1146/annurev.earth.26.1.519.

Garzione, N., G. D. Hoke, J. C. Libarkin, S. Withers, B. MacFadden, J. Eiler, P. Ghosh, and A. Mulch (2008), Rise of the Andes, *Science*, *320*, 1304–1307, doi:10.1126/science.1148615.

Gillis, R. J., B. K. Horton, and M. Grove (2006), Thermochronology, geochronology, and upper crustal structure of the Cordillera Real: Implications for Cenozoic exhumation of the central Andean plateau, *Tectonics*, *25*, TC6007, doi:10.1029/2005TC001887.

Gobierno de Bolivia (1979a), Mapa Geològico de la Region de Anzaldo (Hoja 6440), scale 1:250,000, La Paz.

Gobierno de Bolivia (1979b), Mapa Geològico de la Region de San Pedro (Hoja 6439), scale 1:250,000, La Paz.

Gobierno de Bolivia (1979c), Mapa Geològico de la Region de Surumi (Hoja 6438), scale 1:250,000, La Paz.

Gobierno de Bolivia (1979d), Mapa Geològico de la Region de Vallegrande, scale 1:250,000, La Paz.

González, M., E. Díaz-Martinez, and L. Ticlla (1996), Comentarios sobre la estratigrafia del Silurico y Devonico del norte y centro de la Cordillera Oriental y Altiplano de Bolivia, paper presented at Simposio Sul Americano do Siluro-Devoniano, Ponta Grossa, Brazil.

Gotberg, N., N. McQuarrie, and V. C. Caillaux (2010), Comparison of crustal thickening budget and shortening estimates in southern Peru (12–14°S): Implications for mass balance and rotations in the "Bolivian orocline", *Geol. Soc. Am. Bull.*, *122*, 727–742, doi:10.1130/B26477.1.

Green, P. F. (1981), A new look at statistics in fission track dating, *Nucl. Tracks Radiat. Meas.*, *5*, 77–86, doi:10.1016/0191-278X(81)90029-9.

Green, P. F., I. R. Duddy, A. J. W. Gleadow, P. R. Tingate, and G. M. Laslett (1986), Thermal annealing of fission tracks in apatite: 1. A qualitative description, *Chem. Geol.*, *59*, 237–253.

Gutiérrez-Alonso, G., J. Fernández-Suárez, and A. B. Weil (2004), Orocline triggered lithospheric delamination, in *Orogenic Curvature: Integrating Paleomagnetic and Structural Analyses*, edited by A. J. Sussman and A. B. Weil, *Spec. Pap. Geol. Soc. Am.*, *383*, 121–130.

Gutièrrez-Alonso, G., S. T. Johnston, A. B. Weil, D. Pastor-Galàn, and J. Fernàndez-Suàrez (2012), Buckling an orogen: The Cantabrian Orocline, *GSA Today*, *22*, doi:10.1130/GSATG141A.1.

Henry, S. G., and H. N. Pollack (1988), Terrestrial heat flow above the Andean subduction zone in Bolivia and Peru, *J. Geophys. Res.*, *93*, 15,153–15,162, doi:10.1029/JB093iB12p15153.

Hindle, D., J. Kley, O. Oncken, and S. Sobolev (2005), Crustal balance and crustal flux from shortening estimates in the Central Andes, *Earth Planet. Sci. Lett.*, *230*, 113–124, doi:10.1016/j.epsl.2004.11.004.

Hoorn, C., et al. (2010), Amazonia through time: Andean uplift, climate change, landscape evolution, and biodiversity, *Science*, *330*, 927–931, doi:10.1126/science.1194585.

Horton, B. K. (2005), Revised deformation history of the Central Andes: Inferences from Cenozoic foredeep and intermontane basins of the Eastern Cordillera, Bolivia, *Tectonics*, *24*, TC3011, doi:10.1029/2003TC001619.

Horton, B., B. Hampton, and G. Waanders (2001), Paleogene synorogenic sedimentation in the Altiplano plateau and implications for initial mountain building in the central Andes, *Bull. Geol. Soc. Am.*, *113*, 1387–1400, doi:10.1130/0016-7606(2001)113<1387:PSSITA>2.0.CO;2.

Houseman, G. A., D. P. McKenzie, and P. Molnar (1981), Convective instability of a thickened boundary layer and its relevance for the thermal evolution of continental convergent belts, *J. Geophys. Res.*, *86*, 6115–6132, doi:10.1029/JB086iB07p06115.

Hurford, A. J. (1990), Standardization of fission track dating calibration: Recommendation by the Fission Track Working Group of the I.U.G.S. Subcommission on Geochronology, *Chem. Geol.*, *86*, 171–178.

Isacks, B. L. (1988), Uplift of the Central Andean Plateau and bending of the Bolivian Orocline, *J. Geophys. Res.*, *93*, 3211–3231, doi:10.1029/JB093iB04p03211.

Jonckheere, R., M. Mars, P. Van den Haute, M. Rebetez, and A. Chambaudet (1993), L'apatite de Durango (Mexique): Analyse d'un mineral standard pour la datation par traces de fission, *Chem. Geol.*, *103*, 141–154.

Judge, P. A., and R. W. Allmendinger (2011), Assessing uncertainties in balanced cross sections, *J. Struct. Geol.*, *33*, 458–467, doi:10.1016/j.jsg.2011.01.006.

Ketcham, R. A. (2005), Forward and inverse modeling of low-temperature thermochronometry data, in *Low-Temperature Thermochronology: Techniques, Interpretations, and Applications*, edited by P. W. Reiners and T. A. Ehlers, *Rev. Mineral. Geochem.*, *58*, 275–314, doi:10.2138/rmg.2005.58.11.

Kley, J. (1996), Transition from basement-involved to thin-skinned thrusting in the Cordillera Oriental of southern Bolivia, *Tectonics*, *15*, 763–775.

Kley, J., A. H. Gangui, and D. Krüger (1996), Basement-involved blind thrusting in the Eastern Cordillera, souther Bolivia: Evidence from cross-sectional balancing, gravimetric and magnetotelluric data, *Tectonophysics*, *259*, 171–184, doi:10.1016/0040-1951(95)00067-4.

Kley, J. (1999), Geologic and geometric constraints on a kinematic model of the Bolivian orocline, *J. South Am. Earth Sci.*, *12*, 221–235.

Kley, J., and C. R. Monaldi (1998), Tectonic shortening and crustal thickness in the Central Andes: How good is the correlation?, *Geology*, *26*, 723–726.

Lamb, S. (2000), Active deformation in the Bolivian Andes, South America, *J. Geophys. Res.*, *105*, 25,627–25,653, doi:10.1029/2000JB900187.

Lamb, S., and L. Hoke (1997), Origin of the high plateau in the Central Andes, Bolivia, South America, *Tectonics*, *16*, 623–649, doi:10.1029/97TC00495.

Marshak, S. (2004), Salients, recesses, arcs, oroclines, and syntaxes: A review of ideas concerning the formation of map-view curves in fold-thrust belts, in *Thrust Tectonics and Hydrocarbon Systems*, edited by K. R. McClay, *AAPG Mem., 82*, 131–156.

McQuarrie, N. (2002), The kinematic history of the central Andean fold-thrust belt, Bolivia: Implications for building a high plateau, *Bull. Geol. Soc. Am.*, *114*, 950–963, doi:10.1130/0016-7606(2002)114<0950:TKHOTC>2.0.CO;2.

McQuarrie, N., and P. DeCelles (2001), Geometry and structural evolution of the central Andean backthrust belt, Bolivia, *Tectonics*, *20*, 669–692, doi:10.1029/2000TC001232.

McQuarrie, N., and B. P. Wernicke (2005), An animated tectonic reconstruction of southwestern North America since 36 Ma, *Geosphere*, *1*, 147–172, doi:10.1130/GES00016.1.

McQuarrie, N., J. B. Barnes, and T. A. Ehlers (2008), Geometric, kinematic, and erosional history of the central Andean Plateau, Bolivia (15–17°S), *Tectonics*, *27*, TC3007, doi:10.1029/2006TC002054.

Instituto Geografico Militar (2000), *Digital Atlas of Bolivia*, La Paz, Bolivia.

Mitra, S. (1990), Fault-propagation folds: Geometry, kinematic evolution, and hydrocarbon traps, *AAPG Bull.*, *74*, 921–945.

Moretti, I., P. Baby, E. Mendez, and D. Zubieta (1996), Hydrocarbon generation in relation to thrusting in the Sub Andean zone from 18° to 22°S, Bolivia, *Pet. Geosci.*, *2*, 17–28.

Mueller, J. P., J. Kley, and V. Jacobshagen (2002), Structure and Cenozoic kinematics of the Eastern Cordillera, southern Bolivia, *Tectonics*, *21*(5), 1037, doi:10.1029/2001TC001340.

Namson, J., and S. Mitra (1989), Equal-area balancing, *Am. J. Sci.*, *289*, doi:10.2475/ajs.289.5.563.

Poulsen, C. J., T. A. Ehlers, and N. Insel (2010), Onset of convective rainfall during gradual late Miocene rise of the central Andes, *Science*, *328*, 490–493, doi:10.1126/science.1185078.

Prell, W. L., and J. E. Kutzbach (1992), Sensitivity of the Indian monsoon to forcing parameters and implications for its evolution, *Nature*, *360*, 647–652.

Reiners, P. W., T. L. Spell, S. Nicolescu, and K. A. Zanetti (2004), Zircon (U-Th)/He thermochronometry: He diffusion and comparisons with ^{40}Ar/ ^{39}Ar dating, *Geochim. Cosmochim. Acta*, *68*(8), 1857–1887, doi:10.1016/j.gca.2003.10.021.

Reiners, P. W., T. A. Ehlers, and P. K. Zeitler (2005), Past, present, and future of thermochronology, in *Low Temperature Thermochronology: Techniques, Interpretations, and Applications*, edited by P. W. Reiners and T. A. Whlers, *Rev. Mineral. Geochem.*, *58*, 1–18, doi:10.2138/rmg.2005.58.1.

Riller, U., and O. Oncken (2003), Growth of the central Andean plateau by tectonic segmentation is controlled by the gradient in crustal shortening, *J. Geol.*, *111*, doi:10.1086/373974.

Robinson, D. (2008), Forward modeling the kinematic sequence of the central Himalayan thrust belt, western Nepal, *Geosphere*, *4*, 785–801, doi:10.1130/GES00163.1.

Roeder, D., and R. L. Chamberlain (1995), Structural geology of sub-Andean fold and thrust belt in northwestern Bolivia, in *Petroleum Basins of South America*, edited by A. J. Tankard, R. Suàrez Soruco, and H. J. Welsink, *AAPG Mem.*, *62*, pp. 459–479.

Rogers, J. (1975), Appalachian salients and recesses, *Geol. Soc. Am. Abstr. with Progr.*, 7, I, 111–112.

Roperch, P., T. Sempere, O. Macedo, C. Arriagada, M. Fornari, C. Tapia, M. Garcia, and C. Laj (2006), Counterclockwise rotation of late Eocene-Oligocene fore-arc deposits in southern Peru and its significance for oroclinal bending in the central Andes, *Tectonics*, *25*, TC3010, doi:10.1029/2005TC001882.

Roperch, P., V. Carlotto, G. Ruffet, and M. Fornari (2011), Tectonic rotations and transucrrent deformation south of the Abancay deflection in the Andes of southern Peru, *Tectonics*, *30*, TC2010, doi:10.1029/2010TC002725.

Safran, E. B., A. E. Blythe, and T. Dunne (2006), Spatially variable exhumation rates in orogenic belts: An Andean example, *J. Geol.*, *114*, 665–681, doi:10.1086/507613.

Scheuber, E., D. Mertmann, H. Ege, P. Silva-Gonzalez, C. Heubeck, K. Reutter, and V. Jacobshagen (2006), Exhumation and basin development related to formation of the central Andean Plateau, 21°S, in *The Andes: Active Subduction Orogeny*, edited by O. Oncken et al., pp. 285–301, Springer, Berlin, Germany.

Schmitz, M., and J. Kley (1997), The geometry of the central Andean backarc crust: Joint interpretation of cross section balancing and seismic refraction data, *J. South Am. Earth Sci.*, *10*, 99–110.

Sempere, T. (1994), Kimmeridgian? to Paleocene tectonic evolution of Bolivia, in *Cretaceous Tectonics of the Andes*, edited by J. A. Salfity, pp. 168–212, Vieweg Publishing, Weisbaden, Germany.

Sempere, T. (1995), Phanerozoic evolution of Bolivia and adjacent regions, in *Petroleum Basins of South America*, edited by A. J. Tankard, R. Suàrez Soruco, and H. J. Welsink, *AAPG Mem., 62*, 207–230.

Sempere, T., G. Herail, J. Oller, and M. G. Bonhomme (1990), Late Oligocene-early Miocene major tectonic crisis and related basins in Bolivia, *Geology*, *18*, 946–949, doi:10.1130/0091-7613(1990)0182.3.CO;2.

Sempere, T., G. Carlier, P. Soler, M. Fornari, V. Carlotto, J. Jacay, O. Arispe, D. Néraudeau, J. Cárdenas, S. Rosas, and N. Jiménez (2002), Late Permian—Middle Jurassic lithospheric thinning in Peru and Bolivia and its bearning on Andean-age tectonics, *Tectonophysics*, *345*, 153–181, doi:10.1016/S0040-1951(01)00211-6.

Servicio Geologico de Bolivia (1992), Mapas Tematicos de Recursos Minerales de Bolivia, Uncia (Hoja 6238), scale 1:100,000, La Paz.

Servicio Geologico de Bolivia (1993a), Mapas Tematicos de Recursos Minerales de Bolivia, Chayanta (Hoja 6338), scale 1:100,000, La Paz.

Servicio Geologico de Bolivia (1993b), Mapas Tematicos de Recursos Minerales de Bolivia, Sacaca (Hoja 6339), scale 1:100,000, La Paz.

Servicio Geologico de Bolivia (1994), Mapas Tematicos de Recursos Minerales de Bolivia, Uncia (serie II-MTB-2B), scale 1:250,000, La Paz.

Servicio Geologico de Bolivia (1995), Mapas Tematicos de Recursos Minerales de Bolivia, Cochabamba (serie II-MTB-3B), scale 1:250,000, La Paz.

Sheffels, B. M. (1988), Structural constraints on structural shortening in the Bolivian Andes, PhD thesis, Dep. of Earth Atmos. and Planet. Sci., Mass. Inst. of Techno. Boston, Mass.

Somoza, R., S. Singer, and B. Coira (1996), Paleomagnetism of upper Miocene ignimbrites at the Puna: An analysis of vertical-axis rotations in the Central Andes, *J. Geophys. Res.*, *101*(B5), 11,387–11,400, doi:10.1029/95JB03467.

Somoza, R., S. Singer, and A. Tomlinson (1999), Paleomagnetic study of upper Miocene rocks from northern Chile: Implications for the origin of late Miocene-Recent tectonic rotations in the southern Central Andes, *J. Geophys. Res.*, *104*(B10), 22,923–22,936, doi:10.1029/1999JB900215.

Somoza, R., A. J. Tomlinson, P. J. Caffee, and J. F. Vilas (2012), Paleomagnetic evidence of earliest Paleocene deformation in Calama (~22°S), northern Chile: Andean-type or ridge-collision tectonics?, *J. S. Am. Earth Sci.*, *37*, 208–213, doi:10.1016/j.jsames.2012.04.001.

Springer, M., and A. Forster (1998), Heat-flow density across the Central Andean subduction zone, *Tectonophysics*, *291*, 123–139, doi:10.1016/S0040-1951(98)00035-3.

Suppe, J. (1983), Geometry and kinematics of fault-bend folding, *Am. J. Sci.*, *283*, 684–721.

Tagami, T., and P. B. O'Sullivan (2005), Fundamentals of fission-track thermochronology, in *Low-Temperature Thermochronology: Techniques, Interpretations, and Applications*, edited by P. W. Reiners and T. A. Ehlers, *Rev. Mineral. Geochem.*, *58*, 19–47, doi:10.2138/rmg.2005.58.11.

Taylor, G. K., B. Dashwood, and J. Grocott (2005), Central Andean rotation pattern: Evidence from paleomagnetic rotations of an anomalous domain in the forearc of northern Chile, *Geology*, *33*, 777–780, doi:10.1130/G21876.1.

Taylor, G. K., J. Grocott, B. Dashwood, B. Gipson, and C. Arevalo (2007), Implications for crustal rotation and tectonic evolution in the Central Andes fore arc: New paleomagnetic results from the Copiapo region of northern Chile, 26°–28°S, *J. Geophys. Res.*, *112*, B01102, doi:10.1029/2005JB003950.

Uyeda, S., and T. Watanabe (1982), Terrestrial heat flow in western South America, *Tectonophysics*, *83*, 63–70.

Watts, A. B., S. H. Lamb, J. D. Fairhead, and J. F. Dewey (1995), Lithospheric flexure and bending of the central Andes, *Earth Planet. Sci. Lett.*, *134*, 9–21, doi:10.1016/0012-821X(95)00095-T.

Weil, A. B., and A. J. Sussman (2004), Classifying curved orogens based on timing relationships between structural development and vertical-axis rotations, in *Orogenic Curvature: Integrating Paleomagnetic and Structural Analyses*, edited by A. J. Sussman and A. B. Weil, *Spec. Pap. Geol. Soc. Am., 383*, 1–15.

Welsink, H. J., A. Franco M, and C. Oviedo G. (1995), Andean and pre-Andean deformation, Boomerang Hills area, Bolivia, in *Petroleum Basins of South America*, edited by A. J. Tankard, R. Suàrez Soruco, and H. J. Welsink, *AAPG Mem., 62*, 481–499.

Wigger, P. J., et al. (1994), Variation in the crustal structure of the southern Central Andes deduced from seismic refraction investigations, in *Tectonics of the Southern Central Andes: Structure and Evolution of an Active Continental Margin*, edited by K. J. Reutter et al., pp. 23–48, Springer, New York.

Woodward, N., S. E. Boyer, and J. Suppe (1989), *Balanced Geological Cross-Sections: An Essential Technique in Geological Rsearch and Exploration*, *Short Course Geol.*, vol. 6, AGU, Washington, D.C.

Yonkee, A., and A. B. Weil (2010), Quantifying vertical axis rotation in curved orogens: Correlating multiple data sets with a refined weighted least squares strike test, *Tectonics*, *29*, TC3012, doi:10.1029/2008TC002312.